Crustal seismic imaging of Northeast Tibet using first and later phases of earthquakes and explosions

Crustal seismic imaging of Northeast Tibet using first and later phases of earthquakes and explosions

Anhui Sun,[1,2] Dapeng Zhao,[3] Yuan Gao,[1,2] Qinjian Tian[1,2] and Ning Liu[1,2]

[1]*Key Laboratory of Earthquake Prediction, China Earthquake Administration, Beijing* 100036, *China. E-mail: sah@ief.ac.cn*
[2]*Institute of Earthquake Forecasting, China Earthquake Administration, Beijing* 100036, *China*
[3]*Department of Geophysics, Graduate School of Science, Tohoku University, Sendai* 980–8578, *Japan. E-mail: zhao@tohoku.ac.jp*

SUMMARY

A new crustal 3-D *P*-wave velocity model beneath NE Tibet is determined by jointly inverting 62 339 high-quality first *P* wave and later PmP-wave arrival-time data from local earthquakes and seismic explosions. Resolution tests show that the use of the PmP data can effectively improve the resolution of crustal tomography, especially that of the middle-lower crust. Widespread but intermittent low-velocity anomalies are revealed in the lower crust beneath NE Tibet, and the Kunlun fault acts as a transfer structure. High-velocity zones are visible in most parts of the crust below the transition zones bordering the southwestern Ordos basin between 105° and 106° E longitude. We think that they form an important transpressive boundary to absorb sinistral strike-slip and thrust faulting deformation, like a western front-line of the Ordos basin, which is compatible with the latest GPS observations in the region. Considering the tectonic features and deformation of the Liupanshan fault, we need to pay much attention to the seismic risk of the fault zone from now. Our results reveal different structural features of the major blocks and their boundary faults, indicating the complexity of the Cenozoic crustal deformation in NE Tibet that partitioned between steep strike-slip shear zones and thrust faults.

Key words: Crustal imaging; Seismicity and tectonics; Seismic tomography; Crustal structure.

1 INTRODUCTION

The Tibetan Plateau has dominantly expanded towards the east and northeast in response to the clockwise rigid rotation since India collided with Asia 55 Ma (Tapponnier *et al.* 2001), and the convergence may be absorbed by northeastward shortening at the eastern termination of the Altyn Tagh fault, that forms a transpressive 'horsetail' of grand scale in NE Tibet (Meyer *et al.* 1998). Many geodynamic models have been proposed to explain the structure and tectonic evolution of the Tibetan Plateau (see a review by Yin & Harrison 2000). The northeastern corner of the collision highlands provides the best model of the small, still actively growing and rising, Tibetan Plateau (Tapponnier *et al.* 2001), which is moving towards NE–NNE at a rate of 15–19 mm yr^{-1} relative to the South China block (Gan *et al.* 2007) and counteracted by the North China Craton (Ma 1989), then turned to the southeast sharply. The fundamental mode of continental tectonics has been characterized by two end-member processes: plate-like rigid-body motion and distributed deformation via viscous flow (Zuza & Yin 2016).

Previous studies have shown that low-velocity (low-V) zones in the lower crust beneath the Tibetan Plateau revealed by Rayleigh-wave tomography bound major strike-slip faults in southeastern Tibet (Bao *et al.* 2015b), the Qiangtang and Songpan-Ganze Terranes (Li *et al.* 2014a), pass through the northern limit of the Tibetan Plateau (the Altyn Tagh fault and the Kunlun fault), and extend into the Qaidam basin in the northeastern direction (Bourjot & Romanowicz 1992). The low-V zones are limited by the Qinling north fault zone to the north (Zheng *et al.* 2010), and diminish around the eastern Kunlun fault (Li *et al.* 2012), which are generally consistent with the results of ambient seismic noise and receiver functions (Wu *et al.* 2017). However, the INDEPTH geophysical and geological observations (Nelson *et al.* 1996) showed that the low-viscosity crustal flow in northern Tibet is limited by the Lhasa-Golmud Highway and farther east (Haines *et al.* 2003). Results of the GPS velocity field indicate that the Manyi-Yushu-Xianshuihe fault is a clear northern boundary for the crustal flow (Gan *et al.* 2007).

The north–south seismic zone with the highest level of seismicity in Mainland China extends nearly along 104°E from the Inner
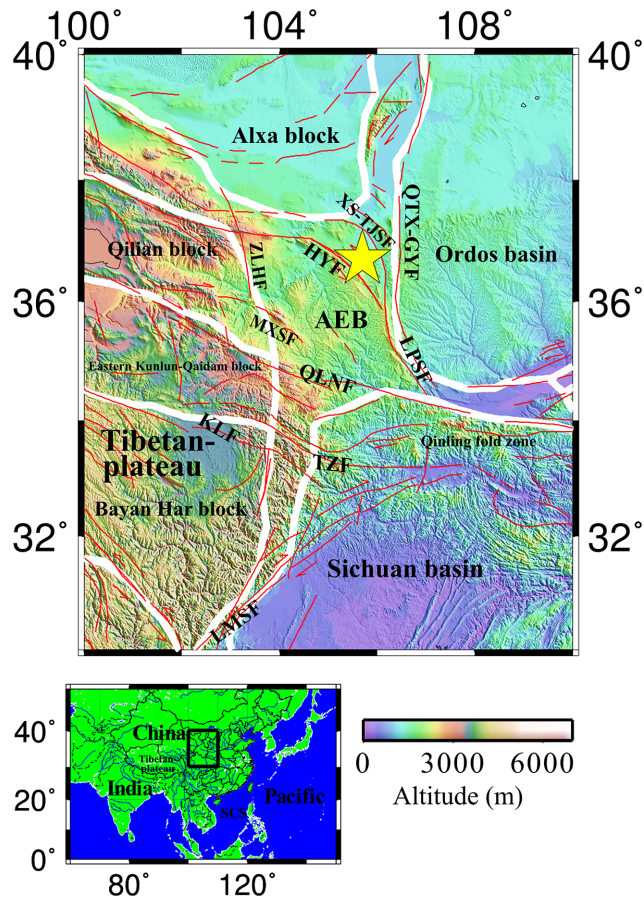
Figure 1. Tectonic background of the study region. The colours represent the surface topography whose scale is shown at the bottom-right. The inset map shows the location of the study region (black box) in Asia. The yellow star denotes the 1920 Haiyuan earthquake (M 8.5). The white thick lines denote boundaries of tectonic blocks (Deng *et al.* 2002; Zhang *et al.* 2003): the Alxa block (ALXB), the Ordos basin (ODB), the eastern tectonic belt of the Tibetan Plateau (AEB), the Qilian block (QLB), the Eastern Kunlun-Qaidam block (EKQB), the Bayan Har block (BYHB), the Qinling fold zone (QLFZ), and the Sichuan basin (SCB). The red lines denote active faults. The major faults are as follows (Ma 1989; Lei & Zhao 2016): the Long-menshan fault (LMSF), the Kunlun fault (KLF), the Tazang fault (TZF), the north Qinling fault (QLNF), the Zhuanlanghe fault (ZLHF), the Maxian-shan fault (MXSF), the Liupanshan fault (LPSF), the Haiyuan fault (HYF), the Xiangshan-Tianjingshan fault (XS-TJSF) and the Qingtongxia-Guyuan fault (QTX-GYF). These abbreviations are shown in this figure and Figures 6-11.

Mongolian District in the north to Yunnan province in the south (Wang *et al.* 1976; Fu *et al.* 1985). It is considered as the tectonic belt (Ma 1989; Wang *et al.* 2015) and main boundary between the eastern and western parts of the Chinese continent, which is also a giant gravity gradient zone with isostatic gravity anomaly and regional magnetic anomaly (Wang *et al.* 2015). Our study region (Fig. 1) is located in the northern part of the north–south seismic zone, where large earthquakes take place frequently (Ma 1989), such as the 1920 Haiyuan earthquake (*M* 8.5) which caused nearly 230 000 fatalities, the 1927 Gulang earthquake (*M* 8.0) and the 2008 Wenchuan earthquake (*M* 8.0). Active tectonic blocks are relatively uniform geologic units that are divided and surrounded by tectonic belts, and have been dynamically active since the late Cenozoic (Zhang *et al.* 2003). There are eight tectonic units (Deng *et al.* 2002; Zhang *et al.* 2003) in our study region (labelled with their full

names in Fig. 1) based on the distribution of fault zones and GPS observations (Wang *et al.* 2001), including the eastern tectonic belt of the Tibetan Plateau (hereafter we call it AEB following Deng *et al.* 2002), that is the transition zone among the Tibetan Plateau, the Alxa block and the Ordos basin.

Whether the large east–west striking sinistral slip faults, including the Haiyuan and Kunlun faults, have acted as rigid-block boundaries or transfer-fault structures linking dip-slip fault systems is an important question to discuss the tectonic mode in northern Tibet (Zuza & Yin 2016). Although relatively fewer studies focused on the crustal structure beneath the northeastern part than the southeastern Tibetan Plateau, previous studies have provided important information on the low-V zones in the crust (e.g. Bour-jot & Romanowicz 1992; Guo *et al.* 2004; Chen *et al.* 2005; Li *et al.* 2006b, 2017; Cheng *et al.* 2014; Tian *et al.* 2014; Wang *et al.* 2016b; Wu *et al.* 2017), including some deep seismic sounding (DSS) experiments (e.g. Li *et al.* 2001, 2002; Zhao *et al.* 2005c; Liu *et al.* 2006; Jia & Zhang 2008). However, the geometric relationships between low-V zones and large faults remain unclear, because the spatial resolution of crustal structure beneath NE Tibet is relatively low (Wang *et al.* 2016a) due to limitations of methods and/or data. For example, teleseismic body-wave data or surface-wave data contain information on both the crustal and upper mantle structures, thus tomographic inversion of the data would bring the influence of the upper mantle to the crust, and costly DSS experiments generally explore the 2-D structures along linear profiles.

The use of crustal reflected waves from the Moho discontinuity (PmP) can effectively improve the resolution of the lower crustal tomography (Jin *et al.* 1999; Zhao *et al.* 2005a; Xia *et al.* 2007; Lei *et al.* 2008; Sun *et al.* 2008; Gupta *et al.* 2009; Wang *et al.* 2018a) without the influence from the deeper structure. In this work, we collected a large number of traveltime data recorded at 154 local seismic stations of the Chinese Provincial Digital Seismic Networks during 1980–2013, 40 broad-band temporary stations of our Seismic Array Cross Hai-Yuan Fault (SACHY) project during 2012–2013 and a 980-km-long DSS experiment. We jointly used the first P (including Pn) and later PmP phase data to determine a new crustal 3-D *P*-wave velocity (*Vp*) model beneath northeastern Tibet. Our new model reveals a detailed distribution of intracrustal low-V zones, which sheds new light on the mechanism of the plateau deformation and expansion.

2 DATA AND METHOD

2.1 Initial velocity model and Moho geometry

A reliable solution of seismic tomography depends on the initial reference model for formulating a linear approximation to a nonlinear inverse problem (Kissling *et al.* 1994). The Moho depth in the study region obtained from several DSS profiles since 1970s ranges from 43 to 64 km. Results of wide-angle reflection profiles show that the average crustal *Vp* at depths from the 5.8 km s^{-1} isoline to the Moho is 6.08–6.27 km s^{-1}, much lower than the global average for the continental regions (6.45 km s^{-1}), which probably reflects a special composition of the crust (Zhang *et al.* 2013). Previous studies of seismic tomography of NE Tibet (e.g. Guo *et al.* 2004; Zheng *et al.* 2010) generally used a global crustal model such as iasp91 (Kennett & Engdahl 1991) with a Moho depth of 24 km or AK135 (Kennett 2005) with a Moho depth of 35 km as the 1-D

starting model for their tomographic inversions, which may affect their inversion results.

In this work, we first derive an optimal 1-D crustal Vp model for our study region from the global crustal model LITHO1.0, which was created by fitting surface wave dispersion results over a wide frequency band (Pasyanos *et al.* 2014). The Moho depth is updated based on a new database of crustal 1-D profiles from active-source seismic studies as well as receiver-function studies, and seismic and gravity results which show that the crust is composed of three distinct layers, that is, the upper crust, the middle crust and the lower crust (Pasyanos *et al.* 2014). Because first arrival data like the refracted Pn phase and the reflected PmP phase are sensitive to the Moho depth, three velocity discontinuities with lateral depth variations deduced from the LITHO1.0 model are taken into account simultaneously in the initial model. Fig. 2(b) shows the Moho geometry in the study region.

To ensure the validity of the Moho depth, we compare the crustal thickness from the LITHO1.0 model in NE Tibet with those from receiver-function results (Pan & Niu 2011; Wang *et al.* 2016b) and DSS data (Li *et al.* 2006a). The Moho depth pattern of LITHO1.0 generally coincides with that of Wang *et al.* (2016b), which becomes shallower from the west to the east consistently in the area (100°–110°E, 32°–40°N). The standard deviation of depth discrepancy is 0.52 km. The Moho depth under the central part along 106° E in the LITHO1.0 model ranges from 50 to 55 km, and it is ∼50 km in the result of Pan & Niu (2011), both are deeper than that by Wang *et al.* (2016b). The Moho depth pattern of LITHO1.0 is generally compatible with that in the DSS result (Li *et al.* 2006a). The exception is in the Qinling north fault zone, around 103°E and 35°N, where the Moho depth in the receiver-function result (Wang *et al.* 2016b) and the LITHO1.0 model ranges from 45 to 50 km, whereas that in the DSS result is from 56 to 60 km. Hence, we deem that LITHO1.0 is a reasonable initial model for our study region.

To further reduce the uncertainties, we conducted a tomographic inversion of our data set using the LITHO1.0 model, and then we obtained a 1-D crustal model by averaging the 3-D inversion results. The obtained 1-D model is shown as the black solid line in Fig. 2a. The average Moho depth is 50.9 km, which is generally consistent with the results of DSS (Zhao *et al.* 2005c) and receiver functions (Wang *et al.* 2016b; Liu *et al.* 2017) in NE Tibet, but much deeper than the Moho depth in the AK135 model (the red line in Fig. 2a) and that in the CRUST2.0 model (the green line in Fig. 2a).

2.2 Data collection

To improve the ray path coverage in the study region, we used three sets of data. The first data set contains local earthquakes that occurred during 1980–2013 and were recorded at 154 local seismic stations of five provincial seismic networks (Fig. 3b) in Gansu, Shanxi and Qinghai Provinces as well as Ningxia and Inner Mongolian Districts, which are compiled by the China Earthquake Network Center (CENC). The second data set contains local earthquakes recorded at 40 portable stations of our SACHY project during 2012–2013 (Fig. 3b), including 40 broad-band sensors (10 Nanometrics Trillium 120P and 15 CMG-3T with bandwidths of 0.02–120 s, and 15 CMG-40T with bandwidths of 0.02–30 s) and Reftek or Taurus data loggers. The third data set is a 980-km long, active-source, refraction and wide-angle reflection profile with 200 DAS-1 seismometers deployed in 1998 by the Research Center of Exploration Geophysics, China Earthquake Administration (CEA)

(Li *et al.* 2002) from Machin in the southwest through Lanzhou to Jingbian in the northeast (hereafter we call it the MLJ profile) across the major tectonic blocks in the study region and the epicentre of the 1920 *M* 8.5 Haiyuan earthquake (Fig. 3b).

An important seismic data source in China is the CENC phase reports that contain *P*-wave arrival times of local earthquakes hand-picked by the CENC staff in the past decades, and the picking accuracy of *P*-wave arrivals is estimated to be 0.05–0.15 s. However, we found some flaws in the phase reports, for example, the information on the focal depths is missing for some events, a same station has different codes and a same event has different origin times determined by different provincial network centres, the hour of the origin time is wrong for some events, etc. We have made great efforts to fix these problems in the CENC reports, and our final data set contains 134 150 arrival-time data from the CENC, including 126 212 first *P* waves and 7938 PmP reflected waves from the Moho. We also collected 8195 *P* arrivals from 754 events recorded at our SACHY stations (the operation No. 1 in Table 1).

To obtain a reliable tomographic result, it is necessary to winnow the data by examining the accuracy of hypocentral parameters and absolute traveltime residuals (i.e. the difference between the observed and calculated traveltimes, Fig. S1f). For this purpose, we relocated all the events by using both *P* and *S* wave data with the optimal 1-D velocity model (Fig. 2a). We only keep the events that have more than eight phase data with traveltime residuals smaller than 2 s (the operations No. 2 and No. 3 in Table 1). The local earthquakes are further winnowed with a specific scheme of selection (Zhao *et al.* 2005a, 2007) according to the maximum number of recording stations and the minimum formal uncertainty of hypocentral parameters (the operation No. 4 in Table 1). We compared the observed traveltimes of *P* and PmP waves with their corresponding theoretical ones computed with the TauP toolkit (Crotwell *et al.* 1999) for the optimal 1-D *Vp* model (Fig. 2a), and the results show that most of the traveltime residuals are smaller than 2 s (Fig. S1f). After the selection, the average number of data at each station is 317. We also added 374 first *P*-wave arrivals and 341 PmP data from nine shots of the DSS profile (e.g. Fig. 4). As a result, our final data set contains 62 339 arrival times from 6602 events, including 58 707 *P* and 3632 PmP data (Table 1), which are used in the tomographic inversion. The ray paths of these data cover the study region densely and uniformly (Fig. 5).

2.3 Tomographic inversion

Seismic later phases such as reflected waves from the Moho discontinuity (PmP) contain important information on the crustal structure, because their ray paths are quite different from those of first *P* waves. Thus, adding the later PmP data can effectively improve crisscrossing and coverage of ray paths in the whole crust, especially in the lower crust, as shown by the previous tomographic studies (Jin *et al.* 1999; Zhao *et al.* 2005a; Xia *et al.* 2007; Lei *et al.* 2008; Sun *et al.* 2008; Gupta *et al.* 2009; Wang *et al.* 2018a). As part of the first arrivals, the head waves (Pn) can be used to investigate the uppermost mantle structure (McNamara *et al.* 1997; Jin *et al.* 1999; Xu *et al.* 2003; Liang *et al.* 2004; Liang & Song 2006). The tomographic method of Zhao *et al.* (2005a) is applied to the first *P* (including Pn) and PmP arrival-time data to determine 3-D *Vp* tomography in the crust of our study region.
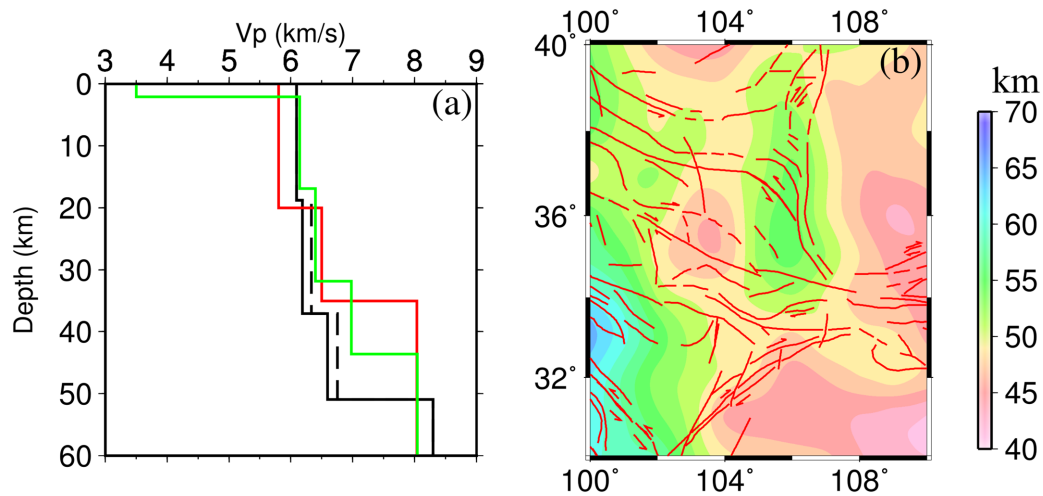
Figure 2. (a) The 1-D crustal *P*-wave velocity (*Vp*) models. The black dashed line denotes the LITHO1.0 model (Pasyanos *et al.* 2014), the black solid line shows a model modified from the LITHO1.0 model (the optimal 1-D model of the present study region), the red solid line shows the AK135 model, whereas the green line shows a model derived from the CRUST2.0 model. (b) The geometry of the Moho discontinuity in the study region derived from the LITHO1.0 model. The Moho depth scale is shown on the right. The red lines denote active faults.
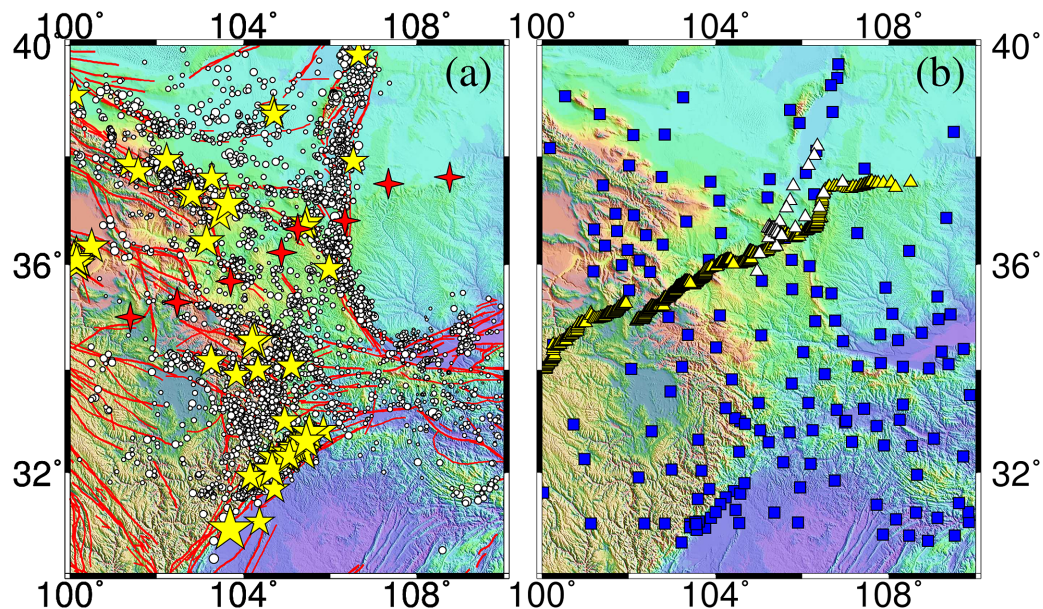

Figure 3. Distribution of the selected seismic events (a) and seismic stations (b) used in this study. In (a), the yellow stars denote earthquakes with magnitudes >5.0 since 1980, whereas the white dots denote events <*M* 5.0. The red polar stars denote nine shots in the deep seismic sounding experiment by the Research Center of Exploration Geophysics, China Earthquake Administration. Note that locations of two of the shots are very close. In (b), the blue squares denote local seismic stations, the yellow triangles denote portable stations along the Machin-Lanzhou-Jingbian (MLJ) profile deployed by Research Center of Exploration Geophysics, and the white triangles denote our SACHY array stations. The other labelling is the same as that in Fig. 1.

Table 1. Data sets used in this study.

| Operation	Seismic stations	Events	*P* phase	PmP phase	Total
1. Data collection and processing	154 CENC local stations (1980–2013)	20 246	126 212	7938	134 150
	40 SACHY portable stations (2012–2013)	754	8195	0	8195
Summary of Operation 1	194 stations	21 000	134 407	7938	142 345
2. Event relocation with residuals <2 s	194	20 809	81 988	5184	87 172
3. Events with >8 phases after Operation 2	194	7014	61 800	3508	65 308
4. Event winnowing after Operation 3	194	6593	58 333	3291	61 624
5. DSS data of the MLJ profile	386	9	374	341	715
Final data set	580	6602	58 707	3632	62 339
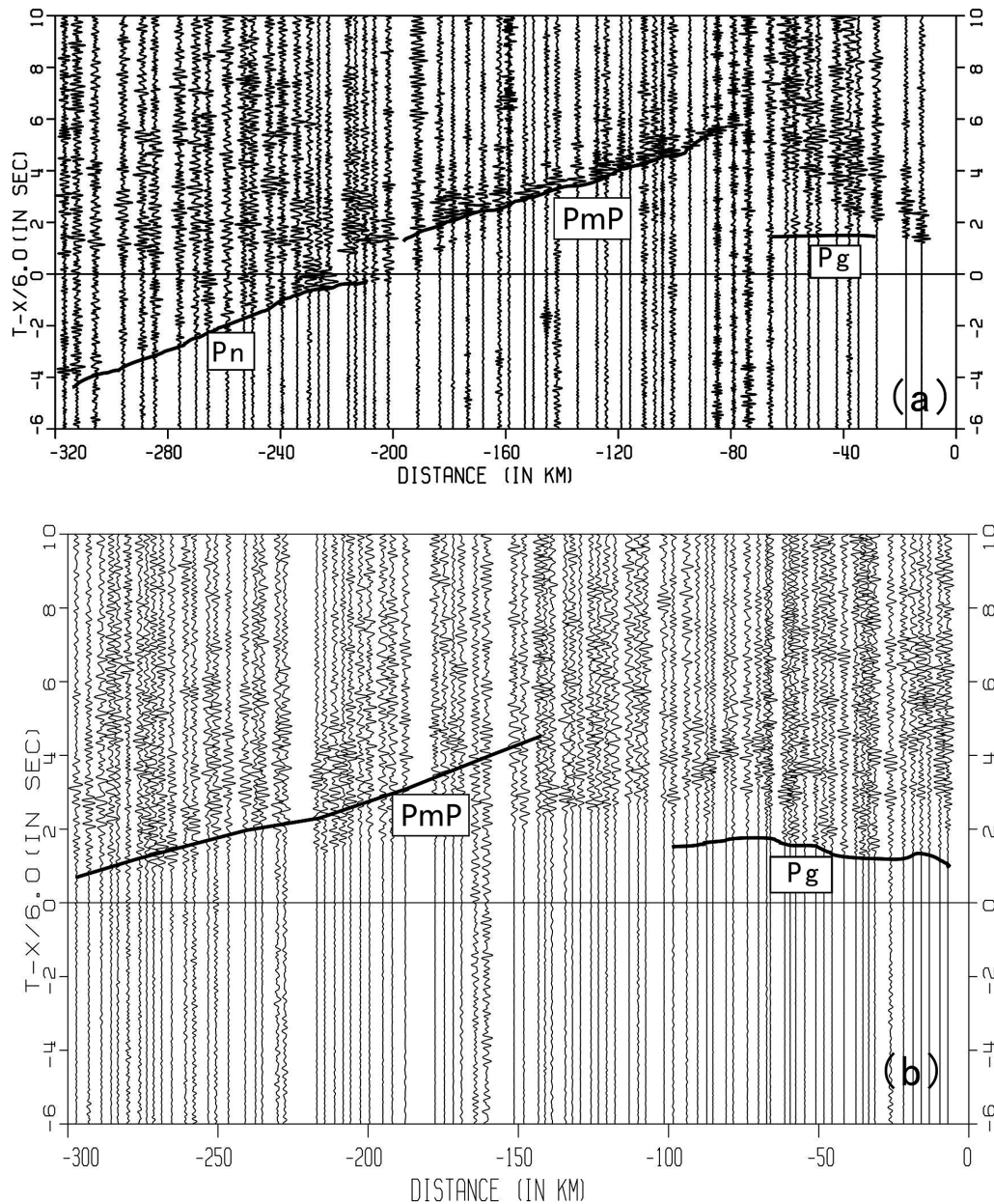
Figure 4. Reduced seismic record sections along the Machin-Lanzhou-Jingbian (MLJ) refraction and wide-angle reflection profile (after Li *et al.* 2002). The seismograms were generated by the shots at (a) Jingbian (SP1032) and (b) Tongxin (SP800).

To express the 3-D *Vp* structure, we set up five layers of grid mesh at depths of 2, 11, 20, 35 and 50 km with a lateral grid interval of 0.35° which represents the lateral resolution scale of the obtained tomographic model. *Vp* perturbations at the grid nodes from the starting 1-D model are taken as unknown parameters. The *Vp* perturbation at any point in the model is calculated by linearly interpolating the *Vp* perturbations at the eight grid nodes surrounding that point. The 3-D ray tracer of Zhao *et al.* (1992) is used to compute theoretical traveltimes and ray paths in the 3-D *Vp* model containing the three undulated velocity discontinuities. A conjugate-gradient type method, the LSQR algorithm (Paige & Saunders 1982) with damping and smoothing regularizations, is used to resolve the large but sparse system of observation equations that relate the arrival-time data to the unknown parameters (Zhao *et al.* 2005a, 2007). The relocated hypocentral parameters (Operation 2 in Table 1) of

the local earthquakes are used to determine *Vp* variations at the 3-D grid nodes in an iterative inversion process (Zhao 2015).

3 ANALYSIS AND RESULTS

Checkerboard resolution tests (CRTs) are conducted to confirm main features of the tomographic result. The procedure to perform a CRT is as follows (Zhao *et al.* 1992, 2005a). First, alternative positive and negative *Vp* anomalies of up to 6 per cent relative to the 1-D velocity model (Fig. 2a) are assigned to the 3-D grid nodes to construct a checkerboard model, then synthetic arrival times are calculated for the checkerboard model with the same numbers of events, stations and ray paths as those in the observed data set. Random noise with a standard deviation of 0.1 s is added to the synthetic arrival times to simulate the picking errors. The
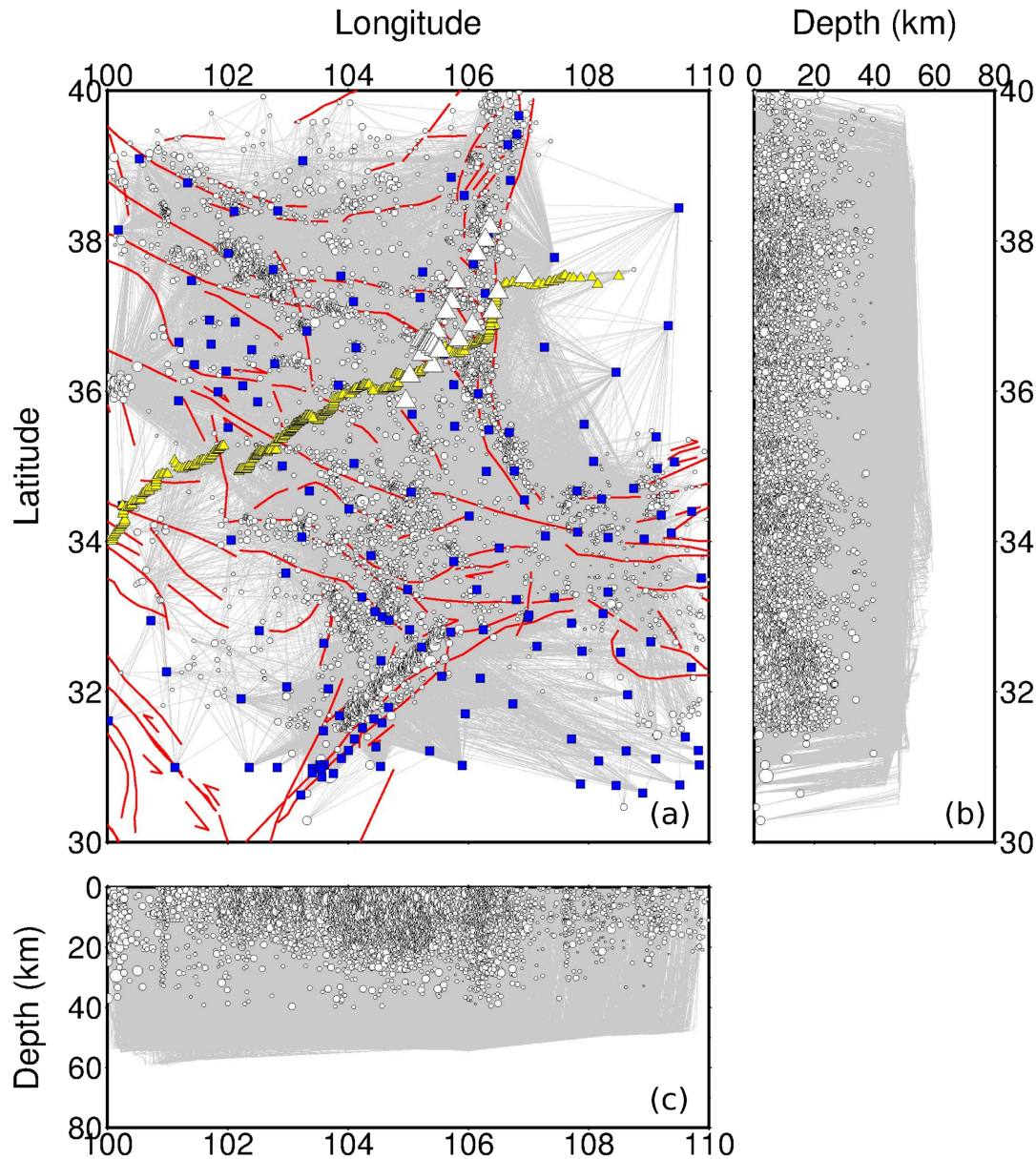
Figure 5. Distribution of ray paths (grey lines) from the 6602 seismic events (white dots) in the study area. Map view (a) and north–south (b) and east–west (c) vertical cross-sections. The blue squares and the white and yellow triangles denote seismic stations used in this study (see Fig. 3b for details). The red lines denote the major active faults in the study region.

synthetic data are then inverted by using the same tomographic method. The resolution is considered to be good in areas where the checkerboard image is well recovered. After conducting CRTs by jointly inverting the *P* and PmP data with different grid intervals (Figs S3–S5), we find that our tomographic model has a lateral resolution of $0.35° \times 0.35°$ in the study region. It is clear that, when both the P and PmP data are used, the ray path coverage is very good in the entire crust (Figs 5 and 10).

To investigate the detailed crustal structure in the source zone of the 1920 Haiyuan earthquake (*M* 8.5), we conducted another CRT along two profiles without interpolation, which are 5.6 and 8.9 km away from the Haiyuan main shock epicentre in longitudinal and latitudinal directions, respectively (Fig S7). The obtained result with the first *P* data has a good resolution in the entire crust (Figs S7a and d). Because there are fewer PmP data than the first

P data, the obtained result with only the PmP data has a lower resolution than that with the first P data (Figs S7b and e). When both the P and PmP data are used, the resolution becomes very good in the whole crust (Figs S7c and f), especially at 35 km depth beneath the Haiyuan hypocentre, thanks to the use of the PmP data.

Fig. 6 shows map views of our tomographic model obtained by jointly inverting the *P* and PmP data. *Vp* variations are revealed at all depths in the crust. The Ordos basin and the Alxa block generally exhibit consistent high-velocity (high-V) anomalies in the entire crust, suggesting that they are stable and rigid blocks. In contrast, the southern border area of the Ordos basin and the southeastern border area of the Alxa block exhibit low-V anomalies at depths of 20–50 km. A distinct high-V zone is revealed in almost the entire crust under eastern AEB, which is connected with the
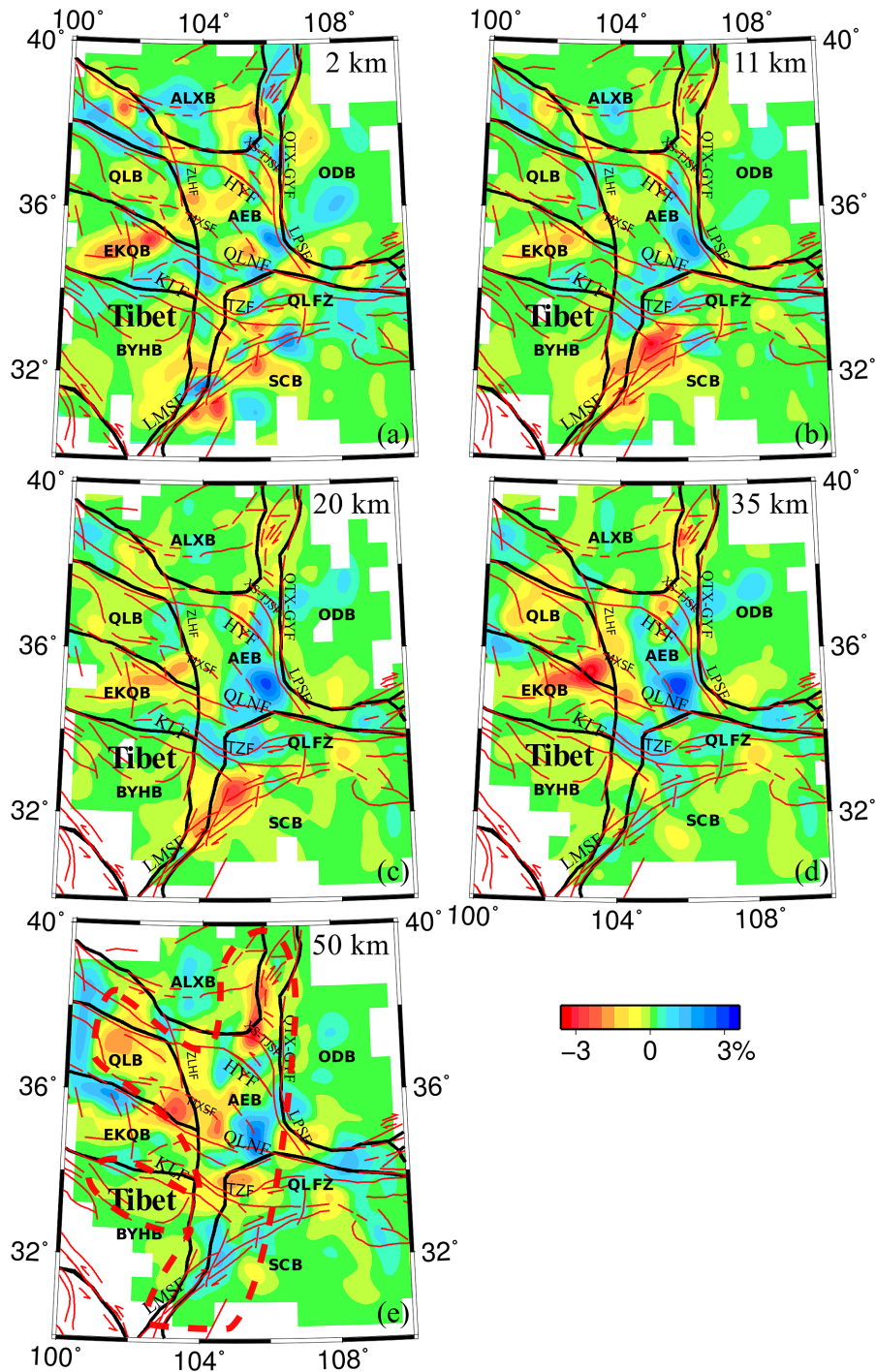
Figure 6. Map views of *P*-wave tomography obtained by a joint inversion of *P* and PmP wave arrival-time data. The layer depth is shown at the upper-right corner of each map. The red and blue colours denote low and high velocity perturbations, respectively, whose scale (in per cent) is shown at the bottom. The black lines denote boundaries of tectonic blocks. The red lines denote active faults.

high-V anomaly under the Ordos basin through the bending part of the Haiyuan fault zone. The NE Tibet block generally exhibits distinct low-V anomalies. Based on very weak reflections identified by the wide-angle seismic experiment, Zhang *et al.* (2013) suggested that a ductile layer with a high attenuation may exist between the crystalline basement (at ∼6 km depth in average) and the Moho (at ∼46 km depth in average) under the central Qilian block. Our tomography reveals a low-V zone in the middle and lower crust of the Qilian block (Figs 6c and d), which is consistent with the result

of double-difference tomography (Xiao & Gao 2017). A significant low-V anomaly is visible under the Eastern Kunlun-Qaidam block, and extends eastward to western AEB at 35 and 50 km depths. A low-V zone is revealed under the eastern Bayan Har block (i.e. the Songpan-Ganzi terrane) and overspreads to the Longmenshan fault zone at 20 km depth. At 50 km depth, a low-V anomaly spreads dispersedly and broadly under the western part of the study region, coinciding with the northern part of the north–south seismic zone
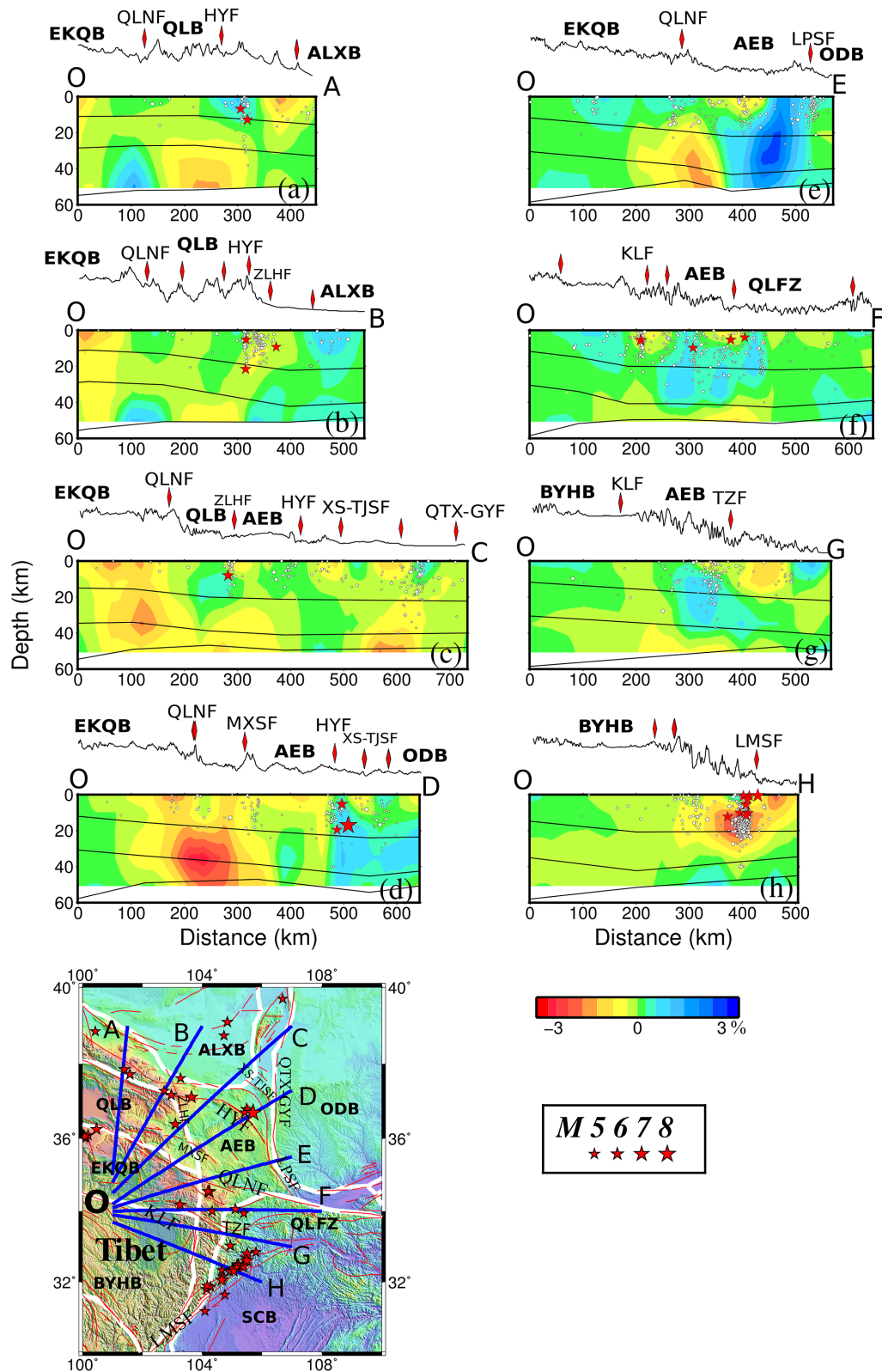
Figure 7. Vertical cross-sections of *P*-wave tomography along the eight profiles shown in the inset map. The three black lines in each section denote the Moho discontinuity and two other velocity boundaries in the crust. The red stars and black dots denote large earthquakes (*M* > 5.0) and smaller events (*M* < 5.0), respectively, within a 25 km width of each profile, which are all relocated using our new 3-D velocity model with more than 10 arrival-time data. The surface topography is shown above each cross-section. The red arrows denote the surface locations of major active faults. The other labelling is the same as that in Fig. 1.
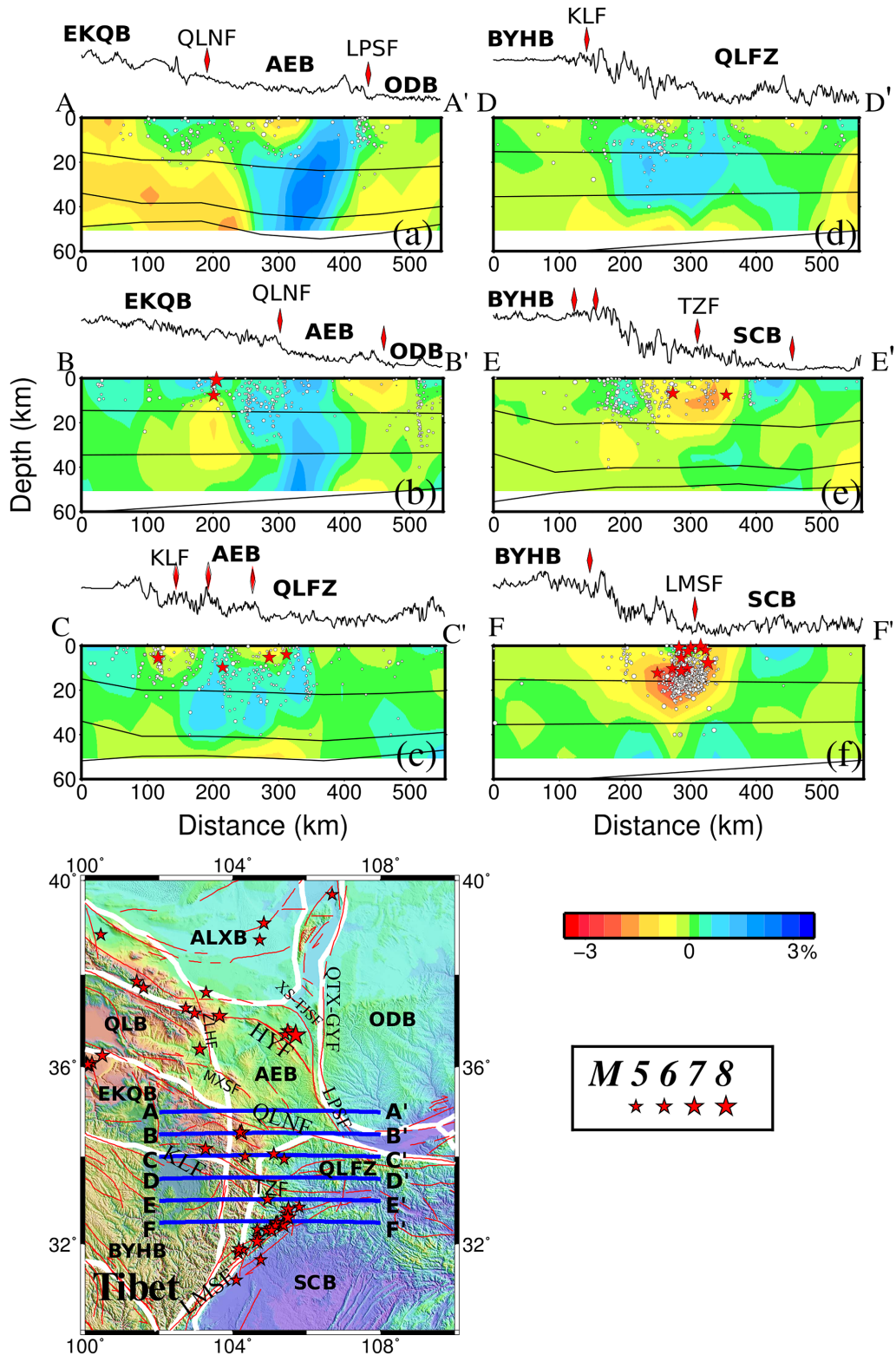
Figure 8. The same as Fig. 7 but along the six profiles shown in the inset map.

(the red dashed line at 50 km depth in Fig. 6) where large earthquakes take place frequently (Ma 1989).

Figs 7 and 8 show some vertical cross-sections of the *Vp* to-mography together with the surface topography and background seismicity along each profile. In Figs 7(a)–(d), a distinct low-V

anomaly is visible in the crust beneath the Eastern Kunlun-Qaidam block and it gradually extends eastward to the lower crust under the high-V zone in the middle-upper crust beneath AEB (Figs 7c, d and f), whereas it is blocked by the high-V anomaly beneath the Haiyuan fault (Fig. 7d) and AEB (Figs 7e and 8a–b). Similarly, a low-V zone
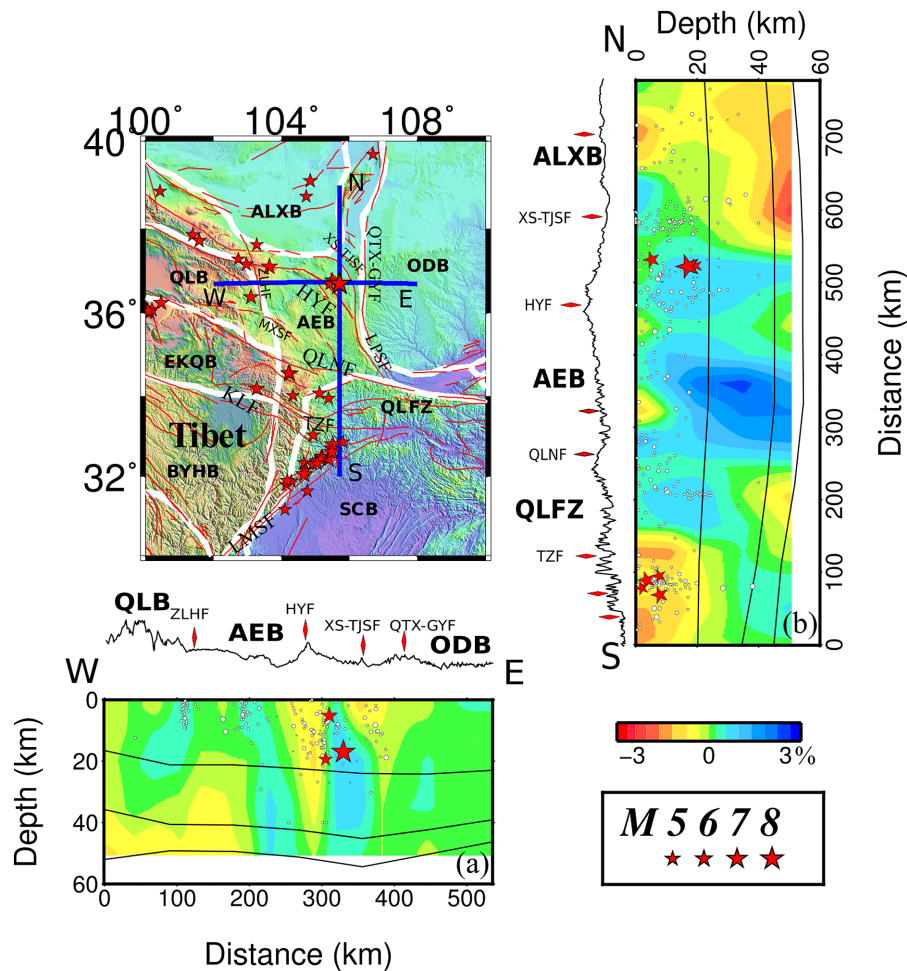
Figure 9. The same as Fig. 7 but along the two profiles shown in the inset map, which pass through the epicentre of the 1920 Haiyuan earthquake (*M* 8.5; the biggest red star).

beneath the Bayan Har block extends eastward to the lower crust under the high-V anomaly in the middle and upper crust beneath the Qinling fold zone (Figs 7g and 8c–d). A high-V feature exists above the low-V anomaly in the lower crust beneath the southern end of AEB at the Kunlun fault and the Tazang fault (Figs 8c and d). To the south of the high-V feature, a low-V anomaly beneath the Bayan Har block warps up eastward to the surface of the Longmenshan fault (Figs 7h and 8f). Similarly, the DSS profile shows a large shovel-like upwelling that dips gently in the lower part but becomes steep in the upper part (Jia *et al.* 2014).

Fig. 9 shows two vertical cross-sections passing through the epicentre of the 1920 Haiyuan earthquake (*M* 8.5). A high-V zone exists in almost the whole crust beneath eastern AEB, which blocks the low-V anomalies in the middle-lower crust beneath the Qilian block (Fig. 9a) and the Qinling fold zone (Fig. 9b). However, the crustal high-V zone beneath northeastern AEB is not connected with that separated by the Haiyuan fault, which exhibits a nearly vertical low-V anomaly from the surface to the uppermost mantle (Fig. 9a). Many faults exist in the southeastern margin of the Alxa block, where significant low-V anomalies exist in the whole crust (Fig. 9b). The 1920 Haiyuan earthquake occurred at the edge of the high-V zone in the upper crust (Figs 7d, 9a and 11c) beneath the southern margin of a quasi tri-junction area (Tian & Ding 1998) which is the intersection of the Haiyuan fault, the Alxa block and the Ordos block. We deem that the Haiyuan earthquake was caused

by the interaction of these adjacent tectonic blocks and faults. The resolution test (Fig. S7) shows that our tomographic images along the profiles (Fig. 9) are reliable.

These tomographic images (Figs 7–9) show that most of the major faults are located at the edge parts of tectonic blocks where *Vp* changes abruptly, such as the north Qinling fault (Figs 7a–d), the Kunlun fault (Fig. 8d), the Haiyuan fault (Figs 7d and 9), the Liupanshan fault (Figs 7d–e and 8a), the Xiangshan-Tianjingshan fault (Figs 7c, d and 9), and the Qingtongxia-Guyuan fault (Fig. 9a). A similar feature is visible at the southern edge of the Alxa block (Figs 7a and 9b). These abrupt *Vp* changes extend from the surface to the deep crust, even down to the uppermost mantle. Most of the relocated earthquakes are distributed in or around the high-V zones, being consistent with the feature of transpressional strike-slip deformation (Tapponnier *et al.* 2001). The Maxianshan and Zhuanglanghe faults show a similar feature with the seismicity in the upper crust (Figs 7b–d). The fault zones at the eastern margin of the Tibetan Plateau mainly exhibit low-V anomalies in the middle-upper crust, such as the Tazang and Longmenshan faults (Figs 7h and 8e–f). A majority of relocated hypocentres are located in the low-V zone in the upper-middle crust beneath the Longmenshan fault, reflecting a listric shape of the Longmenshan fault with an eastward reverse feature (Zhang *et al.* 2008a). We think that these fault zones exhibiting low-V anomalies are weak due to the interaction of adjacent tectonic blocks.
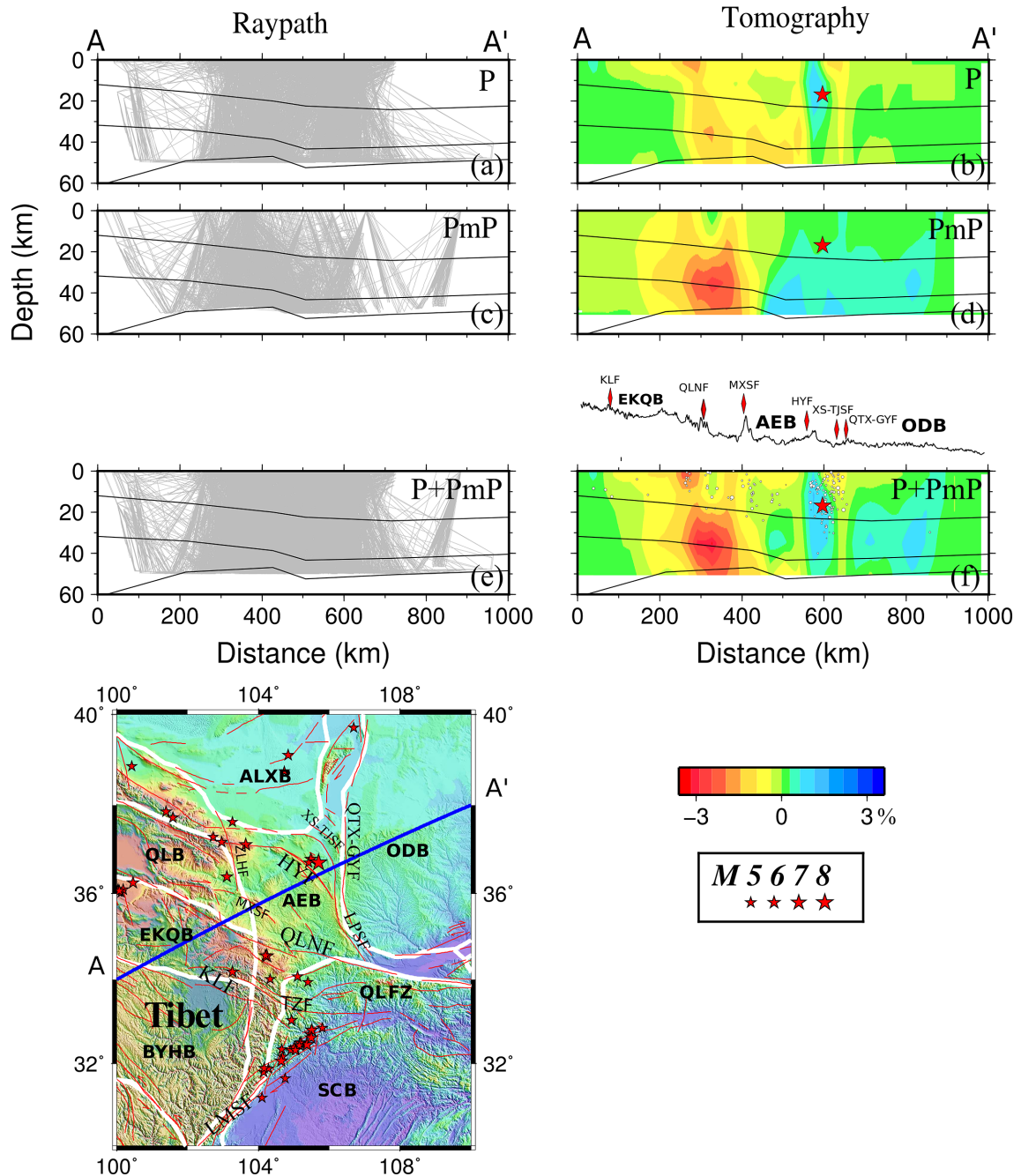
Figure 10. Vertical cross-sections showing the distributions of (a, c, e) ray paths within a 25 km width of the profile A–A' and (b, d, f) *P*-wave tomography along the profile A–A' as shown in the inset map. From the top to the bottom, the data used are the first *P*-wave arrivals (a, b), the PmP-wave arrivals (c, d), and both *P* and PmP arrivals (e, f), respectively. The other labelling is the same as that in Fig. 7.

4 DISCUSSION

4.1 Effects of later phases and discontinuity geometry

To evaluate the effect of the later phase (PmP) data, we conducted a CRT using only the direct *P*-wave data with a lateral grid interval of $0.35° × 0.35°$ (Fig. S6). The result shows that the first *P*-wave data result in a good resolution in the upper crust under the study area where many stations and earthquakes exist, whereas the resolution becomes lower in the middle and lower crust. The addition of PmP data improves the resolution at depths of 20–50 km (Fig. S5), in

particular, in the central and northeastern parts of the study region where our SACHY array and the MLJ profile were deployed (Fig. 3).

DSS experiments with precise blast locations and origin times can help to obtain reliable images of the crust and uppermost mantle (Zhang *et al.* 1995; Jin *et al.* 2011). To investigate the effect of the DSS data, we examine the tomographic images in a vertical cross-section along the MLJ profile (the yellow solid triangles in Fig. 3b) that was deployed across the epicentre of the 1920 Haiyuan earthquake. Fig. 10 shows the distribution of ray paths and the corresponding tomographic images obtained by using the individual data sets of the first *P* and later PmP waves, as well as using both data
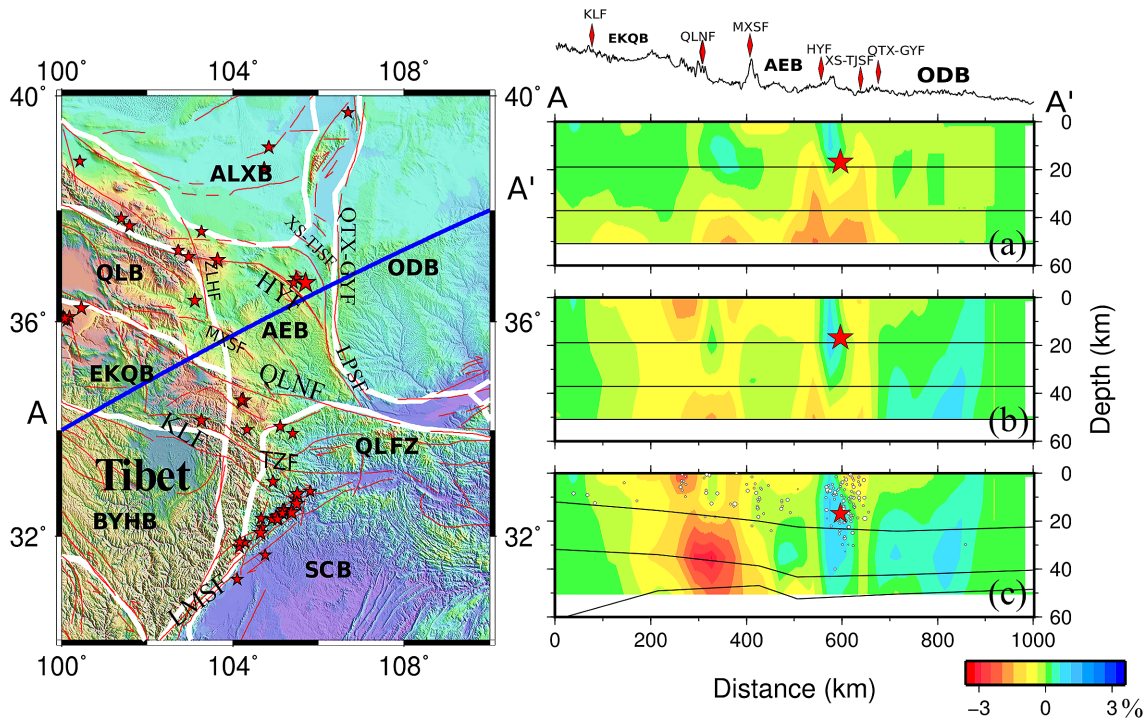
Figure 11. The same as Fig. 10 but for *P*-wave tomography obtained by joint inversions of both the *P* and PmP data. The models in (a, b) are determined when flat velocity discontinuities are adopted. The model in (a) is obtained by inverting only the natural earthquake data. The model in (b) is obtained by inverting both the earthquake data and the DSS data. The model in (c) is the same as that in Fig. 10(f) and is obtained using all the data and with curved velocity discontinuities.

sets. The use of PmP data greatly improves the ray path coverage in the whole crust beneath the MLJ profile. The ray paths of first *P* data (Fig. 10a) are denser than those of the PmP data (Fig. 10b) in the shallow crust at ~200 km away from the edge A of the profile, whereas the *P* rays are sparser below 35 km depth in the lower crust. Hence, the first *P* data are able to reveal low-V anomalies well in the shallow crust, just as the PmP data do in the lower crust. The joint use of the *P* and PmP data leads to better ray crisscrossing and coverage in the whole crust. Jin *et al.* (1999) carried out a joint inversion of *P* and PmP data recorded by the Ningxia regional seismic network. Although the Moho geometry was not considered in their inversion, they found that Pn and PmP data could provide more information on the deep crust where the direct *P* waves cannot reach, and so lead to a better inversion result. However, the Pn and PmP data are sensitive to the Moho depth. Hence in this work, we have taken into account depth variations of the crustal discontinuities including the Moho from the LITHO1.0 model (Pasyanos *et al.* 2014). We also conducted an inversion of the natural earthquake data by assuming the velocity discontinuities to be flat (Fig. 11a). After the DSS data are added, the low-V anomaly in the upper crust beneath the Qinling north fault and the high-V anomalies in the middle crust beneath the Haiyuan fault and the mid-lower crust beneath the Ordos basin could be imaged clearly (Fig. 11b).

As shown in Figs 10 and 11, the Moho discontinuity becomes shallower from Machin in the southwest to Jingbian in the northeast, being consistent with the results of DSS (Li *et al.* 2002) and teleseismic receive functions (Chen *et al.* 2005; Wang *et al.* 2016b). The Moho depth is ~60 km under Machin (Li *et al.* 2002; Chen *et al.* 2005; Wang *et al.* 2016b) and 56 km under the JJA station in AEB (Chen *et al.* 2005). Our tomographic results show that the average *Vp* is lower under the southwestern area than that under the northeastern part, which also coincide with the DSS *Vp* result (Li

et al. 2002) and the receive-function *Vs* result (Chen *et al.* 2005). The Moho discontinuity is a laminated interface with varied depths beneath the Haiyuan fault zone, which is close to a low-V anomaly (Li *et al.* 2002). With the undulant Moho of LITHO1.0 (Fig. 11c), the low-V zones in the mid-lower crust beneath the Qinling north fault and the Maxianshan fault could be clearly revealed, where the Moho depth varies from 48.8 km at (103.25°E, 35.25°N) to 48.1 km at (104.0°E, 35.50°N) by the receiver-function study (Wang *et al.* 2016b). The high-V zone beneath the Haiyuan hypocentre extends to the middle crust (Fig. 11c), where the average Moho depth is 49.7 km (Wang *et al.* 2016b). These results suggest that both the DSS data and the discontinuity geometries can affect the tomographic images.

Our result indicates that the low-V zone beneath the Eastern Kunlun-Qaidam block dips towards the northeast from the surface to the uppermost mantle, extends to the lower crust beneath AEB, and is blocked by the crustal high-V zone beneath the Haiyuan fault. Fig. 6 shows that the crust beneath the central Ordos basin exhibits a high-V anomaly. In its surrounding areas, low-V anomalies exist, which exhibit a high electric conductivity (Tang *et al.* 2005; Zhao *et al.* 2005b; Zhan *et al.* 2017). It was suggested that the high conductivity below 20 km depth may reflect crustal fluids (Tang *et al.* 2005). However, the upper crust beneath the Eastern Kunlun-Qaidam block exhibits a low conductivity (Tang *et al.* 2005). The low-V anomaly in the lower crust of AEB may reflect cracks and fractures caused by the northeastward push of the Tibetan Plateau (Zhan *et al.* 2017). Active faults, such as the Kunlun, Qingtongxia-Guyuan and Haiyuan faults (Xiao & Gao 2017), are located in areas where *Vp* changes abruptly (Figs 7 and 8). The magnetotelluric sounding revealed that these active faults have cut through the whole crust with a steep dip angle (Tang *et al.* 2005).

4.2 Interactions of tectonic blocks

The average crustal velocity of the Alxa block and the Ordos basin is higher than that of the NE Tibetan Plateau, including the Qilian block, the Eastern Kunlun-Qaidam block and the Bayan Har block (Fig. 6). High-V anomalies mainly exist in the crust beneath the central Alxa block, the Ordos basin (Figs 6, 9a and 11c) and the northern margin of the Sichuan basin (Figs 8e and f), suggesting that the Ordos basin (Chang *et al.* 2017) and the Sichuan basin (He & Zheng 2018) are rigid and ancient cratonic blocks with little deformation (Tapponnier *et al.* 1982).

Distinct high-V zones are visible in the middle-lower crust beneath the eastern AEB between 105° and 106° E (Fig. 6), which borders the southwestern Ordos basin. At the northeastern rim of AEB, high-V anomalies are revealed beneath the southern edge of the quasi Tri-junction area (Tian & Ding 1998) and extend to the lower crust like a narrow diamond (Figs 7d, 9a, b and 11c). The latest regional continuous GPS observations show that localized strain accumulation occurs in and around the intersectional region between the Haiyuan fault and the Liupanshan fault (Su *et al.* 2018). The quasi Tri-junction area tends to be northwestward piled out (Tian & Ding 1998) by the composed compressing and shearing among the Alxa block, the Qingtongxia-Guyuan fault and the Haiyuan-Liupanshan fault. The sinistral strike-slip Haiyuan and Xiangshan-Tianjingshan faults appear to pierce through the AEB high-V zones from the surface to the Moho in the northeastern part (Figs 7d, 9a, 10f and 11c), and terminate at the southwestern border of the Ordos basin. Below the Liupanshan strike-slip and thrust fault (Deng *et al.* 1989; Xie *et al.* 2000; Zhang *et al.* 2003), the distinct *Vp* transition zone with abrupt velocity changes (Figs 7e and 8a) is consistent with the southwest-dipping high-conductivity belt (Zhan *et al.* 2017). These *Vp* transition zones below the major faults may illustrate weakening and deformation of blocks caused by the interaction among the Tibetan Plateau, the Alxa block and the Ordos basin (Wang *et al.* 2018b). Strain energy can hardly be accumulated in the weak zone with low-V and high-conductivity, where earthquake faulting would be terminated (Wang *et al.* 2016a). To the south, the AEB high-V zone extends to the uppermost mantle beneath its southeastern parts (Figs 7c–g, 9a–b and 11c) and southern end (Figs 8a and b). Two magnetotelluric sounding profiles (Zhan *et al.* 2014) revealed significant differences between either side of 106°E around the Qinling fold zone, and a shear wave velocity model (Zhang *et al.* 2011) revealed a warm lithosphere boundary at ~105° E longitude which borders the western part from the surface down to 100 km depth. However, our results show that the average *Vp* in eastern AEB is locally higher than that of the adjacent areas in the crust, not exhibiting a gradient zone of transfer-fault structures, but appearing like a wallrock in the non-rigid passive bookshelf-fault model (Zuza & Yin 2016).

In addition, we find that the major *Vp* transition zones dip southwestward to the central Tibetan Plateau beneath the fault zones in southwestern AEB, including the Kunlun fault and the north Qinling fault. The fault zones in northeastern AEB may be even steeper, like the Haiyuan-Liupanshan fault and the Qingtongxia-Guyuan fault. Considering the features of these major active faults with the distribution of relocated earthquakes, the dip angle of the *Vp* transition zones may also reflect the counteract relationship among the adjacent tectonic blocks and transpressional deformation caused by accommodating strike-slip when across the transition area in AEB. We suggest that the internal deformation is generally less intensive in the northeastern margin of the Tibetan Plateau than its central part, which is consistent with the stepwise uplifting of the Tibetan Plateau caused by deformation from the south to the north.

As the young eastward horsetail splayed from the thrusts south of the Altyn Tagh fault (Tapponnier *et al.* 2001), the Haiyuan and Xiangshan-Tianjingshan faults terminated at the southwestern border of the Ordos basin, after encountering with the northeastern rim of AEB. The total velocity decrease from northwest to southeast in the Longxi block was 5.3 mm yr^{-1} within a range of 200 km west of the Liupanshan fault on the horizontal component (Su *et al.* 2018). We infer that the transpressional sinistral strike-slip deformation might be absorbed by transpressive thickening below the northernmost part of AEB. Hence, the noticeable high-V part of AEB could be an important tectonic boundary not only for the blocks, but also for the transpressive deformation accommodating the strike-slip and thrusting motions as a western frontline of the Ordos basin. Previous studies have shown that such connected thrusting and sinistral strike-slip faulting has been a dominant crustal deformation process in Tibet (Tapponnier *et al.* 2001).

4.3 Low-velocity anomalies around the Kunlun fault zone

The distribution of low-V zones plays an important role in intracrustal decollement and shortening that help us understand the mechanisms for evolution of the Tibetan Plateau (Beaumont *et al.* 2004), the convergence and collision of the Tibetan Plateau, the Alxa block and the Ordos basin during the Caledonian orogeny (Zhang *et al.* 2013). Our results show that low-V anomalies widely exist in the crust and uppermost mantle beneath the northeastern and eastern Tibetan Plateau (Fig. 6), which were also partly revealed by Rayleigh-wave tomography (e.g. Yao *et al.* 2005; Li *et al.* 2012, 2014a; Yang *et al.* 2012) and body-wave tomography (e.g. Li *et al.* 2014b; Guo *et al.* 2017; Xiao & Gao 2017). The results of magnetotelluric sounding (Tang *et al.* 2005) suggest that the low-V and high-conductivity structures have a close relationship with the pervasive high-conductivity in the middle-lower crust of the entire Tibetan Plateau, which is possibly attributed to partial melting with a high crustal *Vp/Vs* ratio and high temperature (Wang *et al.* 2008; Wu *et al.* 2017), or a combination of partial melting and salt aqueous fluid (Wei *et al.* 2001; Jin *et al.* 2010). The pervasive low-V anomalies in the mid-lower crust may act like crustal flow, and extrusion of the middle crust probably contributed to the onset of rapid surface uplift of the plateau and crustal thickening in eastern Tibet (Royden *et al.* 2008). However, our results show that the low-V anomalies are not so interconnected in the crust under our study region.

The Kunlun fault in central Tibet transfers eastward and spreads part of the Tibetan plateau into east–west contraction along the Longmenshan fault zone and thrust belt (Yin & Harrison 2000). Li *et al.* (2012) suggested that the low-V zone diminishes around the eastern Kunlun fault. Thrust faults mainly develop north of the Kunlun fault, such as the Amne Machin, Gonghe Nanshan, Lajishan and Qinghai Nanshan faults, whereas strike-slip faults develop in the region south of the Kunlun fault, such as the Mado-Gande fault (Wu *et al.* 2017). Moreover, the *Vp* transition zones below the Kunlun and Tazang faults dip towards the southwest from the surface to the lower crust (Figs 7g and 8d). The Kunlun fault was also detected by the DSS experiment (Zhang *et al.* 2008b) and it cuts through the crust (Liu *et al.* 2017), which may be related to the northward subduction of the Songpan-Ganzi-Hoh-Xil ocean floor beneath the Kunlun batholith that began in the latest Permian and lasted until the latest Triassic in the tectonic evolution of the Himalayan–Tibetan orogen (Zhang & Zheng 1994; Yin & Harrison 2000).

To the north of the Kunlun fault, a distinct low-V zone beneath the northern part of the Eastern Kunlun-Qaidam block dips northeastward into the lower crust of AEB (Figs 7c–e and 8a, b), and is blocked by a high-V zone below eastern AEB. Similarly, a low-V zone beneath the northern margin of the Bayan Har block extends down to the lower crust under the high-V zone below southern AEB (Figs 7g and 8c, d). Li *et al.* (2014b) suggested that there is no crustal flow reaching this area with high-V and low conductivity anomalies in the mid-lower crust beneath the eastern AEB near the western Qinling fold zone. The low-V anomalies in the lower crust and uppermost mantle below AEB may be related to the widespread volcanic deposits interbedded with marine deposits during the late Ordovician to the early Carboniferous (Huang *et al.* 1996; Yin & Harrison 2000). A joint analysis of receiver functions and Rayleigh-wave dispersions (Zheng *et al.* 2015) revealed that the low-V is continuous from the middle-lower crust down to 160 km depth, reflecting an induced local mantle upwelling after partial detachment of the lithosphere (Liu *et al.* 2008). SKS splitting measurements across the NE Tibet show that the fast directions in the crust and upper mantle are generally consistent with each other, suggesting that the crust and upper mantle may have the same deformation (Li *et al.* 2011; Wang *et al.* 2013, 2016b). On the other hand, three mechanisms have been proposed for the hot and deformable crust and the lithosphere in the northern Tibetan Plateau, including convective removal (Molnar *et al.* 1993), subduction-induced upwelling (Tilmann & Ni 2003) and strain heating (McNamara *et al.* 1994).

To the south of the Kunlun fault, GPS results show that a large part of the eastern plateau area is not undergoing shortening in the northeastward convergence direction of the Eastern Himalayan Syntaxis but is stretching (Gan *et al.* 2007). The low-V anomaly in the uppermost mantle below the Bayan Har block (Figs 7g and 8d, e) is consistent with the result of teleseismic *P*-wave tomography (Lei & Zhao 2016), Pn tomography (McNamara *et al.* 1997; Liang & Song 2006) and teleseismic receiver-function analyses (Liu *et al.* 2014). Our results show that the low-V anomaly warps up eastward to the surface of the Longmenshan fault (Figs 7h and 8f), which is consistent with the DSS result (Jia *et al.* 2014) and compatible with the listric shape of the Longmenshan fault with eastward reverse feature (Zhang *et al.* 2008a). A small but significant compressional strain rate component of $\sim$10.5 $\pm$ 2.8 nstrain yr^{-1} exists in a relatively narrow area around the eastern margin (Gan *et al.* 2007). The low-V anomalies in the lower crust may link with lithologic weakening in the mid-lower crust beneath the eastern Tibetan Plateau (Jia *et al.* 2014; Li *et al.* 2014b), causing large earthquakes such as the 2008 Wenchuan earthquake (*M* 8.0).

Therefore, we consider that the Kunlun fault zone has acted as an important tectonic boundary (Chen *et al.* 2005) of transfer-fault structures, which may be the channel for magmatic material upwelling from the deep crust subsequent to the rifting event in the Early Permian (Yin & Harrison 2000) or limited the low-viscosity crustal fluids flowing from the thickened, elevated central plateau (Tapponnier *et al.* 1982; Clark & Royden 2000), just as the *Vs* structure from ambient noise suggested (Li *et al.* 2012; Wu *et al.* 2017). The low-V zone in the northern Tibetan Plateau shows a strong correlation with the region of the mid-Miocene to Quaternary potassic magmatism, suggesting that delamination of lithosphere may have played an important role in the rise of the Tibetan Plateau (Bao *et al.* 2015a). It may be also related to either detachment and deformation of the crust (Liu *et al.* 2014), lithospheric mantle (Liang & Song 2006), or mantle upwelling (Lei & Zhao 2016) that are primarily driven by vertically coherent deformation associated with the India–Asia collision (Wang *et al.* 2016b). Furthermore, the deep

low-V anomaly spreads eastward to the Longmenshan fault zone along the Kunlun fault to the north by the undergoing stretching (Gan *et al.* 2007), which provides a new constraint on the mode of deformation across the Tibetan Plateau (Li *et al.* 2014a) and influences local strain partitioning that controlled the deformation style of the eastern Tibetan Plateau (Liu *et al.* 2014).

4.4 Fault zones and seismicity

In Mainland China, all the great intracontinental earthquakes with *M* > 8.0 and 80–90 per cent of the large earthquakes with *M* > 7.0 occurred at edge parts of tectonic blocks, suggesting that interactions of the blocks directly control the generation of the large earthquakes (Zhang *et al.* 2003). The existence of widespread low-V anomalies indicates that the lower crust and uppermost mantle contain high-temperature materials and fluids related to the northeastward or eastward extension of the Tibetan Plateau, which can reduce the mechanical strength of the seismogenic upper crust (Cheng *et al.* 2014). The low-V zones are mechanically weak no matter they are caused by the crustal flow or partial melting, which is a seismic signature of the intracrustal decollement layer (Zhang *et al.* 2013). Disregarding the low-V anomalies might be caused by either partial melting and salt aqueous fluid (e.g. Wei *et al.* 2001; Tang *et al.* 2005; Jin *et al.* 2010), volcanic deposits and mineral alignment (e.g. Huang *et al.* 1996; Yin & Harrison 2000), or vertically coherent deformation (e.g. Wang *et al.* 2016b), we find that the range of low-V anomalies in the lower crust (the red dashed line at 50 km depth in Fig. 6) coincides well with the northern segment of the north–south seismic zone (Ma 1989). The low-V zones in the lower crust may contain a large amount of fluids, and so they can greatly affect the crustal structure and strength in the source areas of large earthquakes, such as the 2016 *M* 7.3 Kumamoto earthquake (Wang *et al.* 2018a; Zhao *et al.* 2018b) and other large earthquakes in Japan (e.g. Zhao 2015; Zhao *et al.* 2018a). Hence, the low-V zones may play an important role in the crustal seismogenesis.

Significant strain or energy concentration occurs in the fault zones which form boundaries of the tectonic blocks, causing the hazardous earthquakes in the northeastern Tibetan region (Fig. 3a). Interactions of the active faults (Luo & Liu 2010), as well as coseismic and post-seismic deformation of a large earthquake (Xiao & He 2015), can increase Coulomb stress on the neighbouring faults or segments, which may accelerate the occurrence of future earthquakes, such as the 1954 Shandan earthquake (*M* 7.2) and the 1990 Tianzhu earthquake (*M* 6.2) in the study area. Studies of the current stress field show that the Haiyuan fault zone has a strike-slip faulting style, whereas the Liupanshan fault zone exhibits both strike-slip and thrusting faulting components (Deng *et al.* 1989; Xie *et al.* 2000; Zhang *et al.* 2003). The tectonic features and deformation pattern across the Liupanshan fault zone are similar to those of the Longmengshan fault before the 2008 *M* 8.0 Wenchuan earthquake (Zhan *et al.* 2017; Su *et al.* 2018). Hence, we need to pay much attention to the Liupanshan fault zone for its seismic risk in the near future.

5 CONCLUSIONS

In this study, we seek to obtain high-resolution 3-D images of crustal *Vp* structure beneath the northeastern rim of the Tibetan Plateau, with special attention to the detailed distribution of intracrustal low-V zones. Our detailed resolution tests show that the later phase data (PmP) are very useful to improve the reliability of crustal

tomography, especially in the lower crust. Our results shed new light on the complexity of the Cenozoic continental deformation in NE Tibet and may improve our understanding of the geodynamic evolution of the Tibetan Plateau.

The major active faults are located at sharp *Vp* transition zones with abrupt velocity changes at boundaries of tectonic blocks, which reflects the counteracting relationship among the adjacent tectonic blocks. High-velocity zones are visible like crustal wallrock below the transition zones bordering the southwestern Ordos basin between 105° and 106° E longitude, which may become an important tectonic boundary as the western frontline of the Ordos basin that absorbed sinistral strike-slip motion by possibly transpressive deformation. Thus, the Haiyuan and Xiangshan-Tianjingshan faults terminate at the southwestern border of the Ordos basin.

Widespread low-V anomalies are revealed but they are not interconnected in the lower crust beneath NE Tibet. According to the distribution of the low-V anomalies, we suggest that the Kunlun fault acts as an important tectonic boundary of transfer-fault structures. Although we cannot tell the origin of the low-V zones, they coincide well with the northern segment of the north–south seismic zone in the lower crust. The low-V zones may be a key factor in the deep crust affecting the earthquake generation. Furthermore, considering the tectonic features and regional fault interactions, we need to pay much attention to the seismic risk of the Liupanshan fault zone in the near future.

ACKNOWLEDGEMENTS

REFERENCES

Bao, X. *et al.*, 2015b. Two crustal low-velocity channels beneath SE Tibet revealed by joint inversion of Rayleigh wave dispersion and receiver functions, *Earth planet. Sci. Lett.,* **415,** 16–24.

Bao, X., Song, X. & Li, J., 2015a. High-resolution lithospheric structure beneath Mainland China from ambient noise and earthquake surface-wave tomography, *Earth planet. Sci. Lett.,* **417,** 132–141.

Beaumont, C., Jamieson, R.A., Mai, H.N. & Medvedev, S., 2004. Crustal channel flows: 1. Numerical models with applications to the tectonics of the Himalayan-Tibetan orogen, *J. geophys. Res.,* **109**(B6), B06406.

Bourjot, L. & Romanowicz, B., 1992. Crust and upper mantle tomography in Tibet using surface waves, *Geophys. Res. Lett.,* **19**(9), 881–884.

Chang, L., Ding, Z., Wang, C. & Flesch, L.M., 2017. Vertical coherence of deformation in lithosphere in the NE margin of the Tibetan plateau using GPS and shear-wave splitting data, *Tectonophysics,* **699,** 93–101.

Cheng, B., Cheng, S., Zhang, G. & Zhao, D., 2014. Seismic structure of the Helan–Liupan–Ordos western margin tectonic belt in North-Central

China and its geodynamic implications, *J. Asian Earth Sci.,* **87**(12), 141–156.

Chen, J., Liu, Q., Li, S., Guo, B. & Lai, Y., 2005. Crust and upper mantle S-wave velocity structure across Northeastern Tibetan Plateau and Ordos Block, *Chinese. J. Geophys. (in Chinese),* **48**(2), 369–379.

Clark, M.K. & Royden, L.H., 2000. Topographic ooze: building the eastern margin of Tibet by lower crustal flow, *Geology,* **28**(8), 703–706.

Crotwell, H.P., Owens, T.J. & Ritsema, J., 1999. The TauP Toolkit: Flexible Seismic Travel-time and Ray-path Utilities, *Seismol. Res. Lett.,* **70**(2), 154–160.

Deng, Q., Zhang, P., Ran, Y., Yang, X., Wei, M. & Chu, Q., 2002. General characteristics of China active tectonics, *Sci. China, Ser. D: Earth Sci.,* **32**(12), 1020–1030.

Deng, Q. *et al.*, 1989. Haiyuan strike-slip fault zone and its compressional structures of the end, *Seismol. Geol.,* **11**(1), 1–14.

Fu, C., Chen, Y. & Qi, G., 1985. *Fundamentals of Geophysics (in Chinese),* pp. 286–291, Science Publishing House.

Gan, W., Zhang, P., Shen, Z.K., Niu, Z., Wang, M., Wan, Y., Zhou, D. & Cheng, J., 2007. Present-day crustal motion within the Tibetan Plateau inferred from GPS measurements, *J. geophys. Res.,* **112**(B8), B08416.

Guo, B., Liu, Q., Chen, J., Zhao, D., Li, S. & Lai, Y., 2004. Seismic tomographic imaging of the crust and upper mantle beneath the northeastern edge of the Qinghai-Xizang plateau and the ordos area, *Chinese. J. Geophys. (in Chinese),* **47**(5), 892–899.

Guo, H.L., Ding, Z.F. & Xiao-Ming, X.U., 2017. Upper mantle structure beneath the northern South-Nouth Seismic Zone from teleseismic traveltime data, *Chinese. J. Geophys. (in Chinese),* **60**(1), 86–97.

Gupta, S., Zhao, D., Ikeda, M., Ueki, S. & Rai, S., 2009. Crustal tomography under the Median Tectonic Line in Southwest Japan using P and PmP data, *J. Asian Earth Sci.,* **35**(5), 377–390.

Haines, S.S., Klemperer, S.L., Brown, L., Guo, J., Mechie, J., Meissner, R., Ross, A. & Zhao, W., 2003. INDEPTH III seismic data: From surface observations to deep crustal processes in Tibet, *Tectonics,* **22**(1), 1001.

He, C. & Zheng, Y., 2018. Seismic evidence for the absence of deeply subducted continental slabs in the lower lithosphere beneath the Central Orogenic Belt of China, *Tectonophysics,* **723,** 178–189.

Huang, H., Huang, Q. & Ma, Y., 1996. *Geology of Qaidam Basin and its Petroleum Prediction (in Chinese),* pp. 357, Geological Publishing House.

Jia, S. & Zhang, X., 2008. A study on the crust phases of deep seismic sounding and the fine crust structure in the northeast margin of Tibetan plateau, *Chinese. J. Geophys. (in Chinese),* **51**(5), 1000–1014.

Jia, S.X. *et al.*, 2014. The crustal structures of the central Longmenshan along and its margins as related to the seismotectonics of the 2008 Wenchuan Earthquake, *Sci. China Earth Sci.,* **57**(4), 777–790.

Jin, C., Zhao, W., Chen, X. & Cai, X., 2011. Inversion of earthquake and explosion data for 3-D velocity structure in Ningxia and adjacent region, *Acta Seismol. Sin.,* **33**(5), 614–623.

Jin, S., Wei, W., Wang, S., Ye, G., Deng, M. & Tan, H., 2010. Discussion of the formation and dynamic signification of the high conductive layer in Tibetan crust, *Chinese. J. Geophys. (in Chinese),* **53**(10), 2376–2385.

Jin, Y., Yang, M., Zhao, W., Shi, X., Xu, W. & Li, G., 1999. Inversion of 3-D crustal P-wave velocity structure in Ningxia and its neighborhood by using direct, reflected and refracted waves, *Earthq. Sci.,* **12**(4), 436–446.

Kennett, B.L.N., 2005. *Seismological Tables: ak135,* The Australian National University.

Kennett, B.L.N. & Engdahl, E.R., 1991. Traveltimes for global earthquake location and phase identification, *Geophys. J. R. astr. Soc.,* **105**(2), 429–465.

Kissling, E., Ellsworth, W.L., Eberhart-phillips, D. & Kradolfer, U., 1994. Initial Reference Models in Local Earthquake Tomography, *J. geophys. Res.,* **99**(B10), 19 635–19 646.

Lei, J., Xie, F., Lan, C., Xing, C. & Ma, S., 2008. Seismic images under the Beijing region inferred from P and PmP data, *Phys. Earth planet. Inter.,* **168**(3–4), 134–146.

Lei, J. & Zhao, D., 2016. Teleseismic P-wave tomography and mantle dynamics beneath Eastern Tibet, *Geochem. Geophys. Geosyst.,* **17,** 1861–1884.

Liang, C. & Song, X., 2006. A low velocity belt beneath northern and eastern Tibetan Plateau from Pn tomography, *Geophys. Res. Lett,* **33,** L22306.

Liang, C., Song, X. & Huang, J., 2004. Tomographic inversion of Pn travel times in China, *J. geophys. Res,* **109**(B11304), B11304.

Li, H., Li, S., Song, X., Gong, M., Li, X. & Jia, J., 2012. Crustal and uppermost mantle velocity structure beneath northwestern China from seismic ambient noise tomography, *Geophys. J. Int.,* **188**(1), 131–143.

Li, H., Shen, Y., Huang, Z., Li, X., Gong, M., Shi, D., Sandvol, E. & Li, A., 2014a. The distribution of the mid-to-lower crustal low-velocity zone beneath the northeastern Tibetan Plateau revealed from ambient noise tomography, *J. geophys. Res.,* **119**(3), 1954–1970.

Li, S., Mooney, W.D. & Fan, J., 2006a. Crustal structure of mainland China from deep seismic sounding data, *Tectonophysics,* **420**(1–2), 239–252.

Li, S., Zhang, X., Zhang, C., Zhao, J. & Cheng, S., 2002. A preliminary study on the crustal velocity structure of Maqin-Lanzhou-Jingbian by means of deep seismic sounding profile, *Chinese. J. Geophys. (in Chinese),* **45**(2), 210–217.

Li, S. *et al.*, 2001. Seismic sounding profile and its interpretation in the region of Xiji-Zhongwei, *Seismol. Geol.,* **23**(1), 86–92.

Liu, M., Li, S., Fang, S., Fan, J. & Li, Z., 2008. Study on crustal composition and geodynamics using seismic velocities in the northeastern margin of the Tibetan plateau, *Chinese. J. Geophys. (in Chinese),* **51**(2), 378–382.

Liu, M., Mooney, W.D., Li, S., Okaya, N. & Detweiler, S., 2006. Crustal structure of the northeastern margin of the Tibetan plateau from the Songpan-Ganzi terrane to the Ordos basin, *Tectonophysics,* **420**(1), 253–266.

Liu, Q. *et al.*, 2014. Eastward expansion of the Tibetan Plateau by crustal flow and strain partitioning across faults, *Nat. Geosci.,* **7**(5), 361–365.

Liu, Z. *et al.*, 2017. New images of the crustal structure beneath eastern Tibet from a high-density seismic array, *Earth planet. Sci. Lett.,* **480**, 33–41.

Li, Y., Wang, X., Zhang, R., Wu, Q. & Ding, Z., 2017. Crustal structure across the NE Tibetan Plateau and Ordos Block from the joint inversion of receiver functions and Rayleigh-wave dispersions, *Tectonophysics,* **705**, 33–41.

Li, Y., Wu, Q., An, Z., Tian, X., Zeng, R. & Zhang, R., 2006b. The Poisson ratio and crustal structure across the NE Tibetan Plateau determined from receiver functions, *Chinese. J. Geophys. (in Chinese),* **49**(5), 1359–1368.

Li, Y., Wu, Q., Zhang, F., Feng, Q. & Zhang, R., 2011. Seismic anisotropy of the Northeastern Tibetan Plateau from shear wave splitting analysis, *Earth planet. Sci. Lett.,* **304**(1), 147–157.

Li, Z., Ni, S. & Roecker, S., 2014b. Interstation Pg and Sg differential traveltime tomography in the northeastern margin of the Tibetan plateau: implications for spatial extent of crustal flow and segmentation of the Longmenshan fault zone, *Phys. Earth planet. Inter.,* **227**(1), 30–40.

Luo, G. & Liu, M., 2010. Stress evolution and fault interactions before and after the 2008 Great Wenchuan earthquake, *Tectonophysics,* **491**(1–4), 127–140.

Ma, X., 1989. *Lithospheric Dynamics Atlas of China (in Chinese),* pp. 29–30, China Cartographic Publishing House.

McNamara, D.E., Owens, T.J., Silver, P.G. & Wu, F.T., 1994. Shear wave anisotropy beneath the Tibetan Plateau, *J. geophys. Res.,* **99**(B7), 13655–13665.

McNamara, D.E., Walter, W.R., Owens, T.J. & Ammon, C.J., 1997. Upper mantle velocity structure beneath the Tibetan Plateau from Pn travel time tomography, *J. geophys. Res.,* **102**(B1), 493–505.

Meyer, B., Tapponnier, P., Bourjot, L., Metivier, F., Gaudemer, Y., Peltzer, G., Guo, S. & Chen, Z., 1998. Crustal thickening in Gansu-Qinghai, lithospheric mantle subduction, and oblique, strike-slip controlled growth of the Tibet plateau, *Geophys. J. Int.,* **135**(1), 1–47.

Molnar, P., England, P. & Martinod, J., 1993. Mantle dynamics, uplift of the Tibetan Plateau, and the Indian Monsoon, *Rev. Geophys.,* **31**(4), 357–396.

Nelson, K.D. *et al.*, 1996. Partially molten middle crust beneath southern Tibet: synthesis of project INDEPTH results, *Science,* **274**(5293), 1684.

Paige, C.C. & Saunders, M.A., 1982. LSQR: An algorithm for sparse linear equations and sparse least squares, *ACM Trans. Math. Softw.,* **8**(1), 43–71.

Pan, S. & Niu, F., 2011. Large contrasts in crustal structure and composition between the Ordos plateau and the NE Tibetan plateau from receiver function analysis, *Earth planet. Sci. Lett.,* **303**(3–4), 291–298.

Pasyanos, M.E., Masters, T.G., Laske, G. & Ma, Z., 2014. LITHO1.0: an updated crust and lithospheric model of the Earth, *J. geophys. Res.,* **119**(3), 2153–2173.

Royden, L.H., Burchfiel, B.C. & van der Hilst, R.D., 2008. The geological evolution of the Tibetan Plateau, *Science,* **321**(5892), 1054–1058.

Sun, A., Zhao, D., Ikeda, M., Chen, Y. & Chen, Q., 2008. Seismic imaging of southwest Japan using P and PmP data: Implications for arc magmatism and seismotectonics, *Gondwana Res.,* **14**(3), 535–542.

Su, X., Yao, L., Wu, W., Meng, G., Su, L., Xiong, R. & Hong, S., 2018. Crustal deformation on the northeastern margin of the Tibetan plateau from continuous GPS observations, *Remote Sens.,* **11**(1), 34.

Tang, J., Zhan, Y., Zhao, G., Deng, Q., Wang, J., Chen, X., Zhao, J. & Xuan, F., 2005. Electrical conductivity structure of the crust and upper mantle in the northeastern margin of the Qinghai-Tibet plateau along the profile Maqên-Lanzhou-Jingbian, *Chinese. J. Geophys. (in Chinese),* **48**(5), 1205–1216.

Tapponnier, P., Peltzer, G., Le Dain, A., Armijo, R. & Cobbold, P., 1982. Propagating extrusion tectonics in Asia: new insights from simple experiments with plasticine, *Geology,* **10**(12), 611–616.

Tapponnier, P., Xu, Z., Roger, F., Meyer, B., Arnaud, N., Wittlinger, G. & Yang, J., 2001. Oblique stepwise rise and growth of the Tibet Plateau, *Science,* **294**(5547), 1671–1677.

Tian, Q. & Ding, G., 1998. The tectonic feature of a quasi tri-junction in the northeastern corner of Qinghai-Xizang plateau, *Earthq. Res. in China,* **14**(4), 27–35.

Tian, X., Liu, Z., Si, S. & Zhang, Z., 2014. The crustal thickness of NE Tibet and its implication for crustal shortening, *Tectonophysics,* **634**, 198–207.

Tilmann, F. & Ni, J., 2003. Seismic imaging of the downwelling Indian lithosphere beneath central Tibet, *Science,* **300**(5624), 1424–1427.

Wang, C., Li, Y. & Lou, H., 2016a. Issues on crustal and upper-mantle structures associated with geodynamics in the northeastern Tibetan Plateau, *Chin. Sci. Bull. (in Chinese),* **61**(20), 2239–2263.

Wang, C. *et al.*, 2008. S-wave crustal and upper mantle's velocity structure in the eastern Tibetan Plateau — Deep environment of lower crustal flow, *Sci. China (in Chinese),* **51**(2), 263–274.

Wang, C.Y., Yang, W.C., Wu, J.P. & Ding, Z.F., 2015. Study on the lithospheric structure and earthquakes in North-South Tectonic Belt, *Chinese. J. Geophys. (in Chinese),* **58**(11), 3867–3901.

Wang, H., Zhao, D., Huang, Z., Xu, M., Wang, L., Nishizono, Y. & Inakura, H., 2018a. Crustal tomography of the 2016 Kumamoto earthquake area in West Japan using P and PmP data, *Geophys. J. Int.,* **214**, 1151–1163.

Wang, Q., Gao, Y., Shi, Y.T. & Wu, J., 2013. Seismic anisotropy in the uppermost mantle beneath the northeastern margin of Qinghai-Tibet plateau: evidence from shear wave splitting of SKS, PKS and SKKS, *Chinese J. Geophys. (in Chinese),* **56**, 892–905.

Wang, Q., Niu, F., Gao, Y. & Chen, Y., 2016b. Crustal structure and deformation beneath the NE margin of the Tibetan plateau constrained by teleseismic receiver function data, *Geophys. J. Int.,* **204**(1), 167–179.

Wang, Q. *et al.*, 2001. Present-Day crustal deformation in China constrained by global positioning system measurements, *Science,* **294**(5542), 574–577.

Wang, S. *et al.*, 2018b. Crustal P-wave velocity structure in the northeastern margin of the Qinghai-Tibetan Plateau and insights into crustal deformation, *Sci. China,* **61**(9), 1221–1237, https://doi.org/10.1007/s11430-017-9227-7.

Wang, Z.S., Wang, Z.Y., Gu, J.P. & Xiong, X.Y., 1976. A preliminary investigation of the limits and certain features of the North-South seismic zone of China, *Chinese J. Geophys. (in Chinese),* **19**, 110–117

Wei, W. *et al.*, 2001. Detection of widespread fluids in the Tibetan crust by magnetotelluric studies, *Science,* **292**(5517), 716.

Wessel, P. & Smith, W.H.F., 1998. New version of generic mapping tools released, *EOS, Trans. Am. geophys. Un.,* **79**, 579.

Wu, Z., Xu, T., Badal, J., Yao, H., Wu, C. & Teng, J., 2017. Crustal shear-wave velocity structure of NE Tibet revealed by ambient seismic noise and receiver functions, *Gondwana Res.,* **41**, 400–410.

Xiao, J. & He, J., 2015. 3D finite-element modeling of earthquake interaction and stress accumulation on main active faults around the northeastern

Tibetan Plateau edge in the past ∼100 years, *Bull. seism. Soc. Am.,* **105**(5), 256–266.

Xiao, Z. & Gao, Y., 2017. Crustal velocity structure beneath the northeastern Tibetan plateau and adjacent regions derived from double difference tomography, *Chinese. J. Geophys. (in Chinese),* **60**(6), 2213–2225.

Xia, S., Zhao, D., Qiu, X., Nakajima, J., Matsuzawa, T. & Hasegawa, A., 2007. Mapping the crustal structure under active volcanoes in central Tohoku, Japan using P and PmP data, *Geophys. Res. Lett.,* **34**(10), L10309.

Xie, F., Shu, S., Dou, S. & Zhang, S., 2000. Seismic tectonic stress field in the region of Haiyuan-Liupanshan fault zone to Yinchuan fault depression, *Seismology and Geology,* **22**(2), 139–146.

Xu, Z., Wang, S. & Pei, S., 2003. Lateral Variation of Pn velocity beneath northeastern marginal region of Qinghai-Xizang plateau, *Earthq. Sci.,* **16**(1), 26–33.

Yang, Y., Ritzwoller, M.H., Zheng, Y., Shen, W., Levshin, A.L. & Xie, Z., 2012. A synoptic view of the distribution and connectivity of the midcrustal low velocity zone beneath Tibet, *J. geophys. Res.,* **117**(B04303), 1–20.

Yao, H., Xu, G., Zhu, L. & Xiao, X., 2005. Mantle structure from interstation Rayleigh wave dispersion and its tectonic implication in western China and neighboring regions, *Phys. Earth planet. Inter.,* **148**(1), 39–54.

Yin, A. & Harrison, T.M., 2000. Geologic evolution of the Himalayan-Tibetan orogen, *Annu. Rev. Earth planet. Sci.,* **28**(1), 211–280.

Zhang, P., Deng, Q., Zhang, G., Ma, J., Gan, W., Min, W., Mao, F. & Wang, Q., 2003. Active tectonic blocks and strong earthquakes in the continent of China, *Sci. China (in Chinese),* **46**(2), 13–24.

Zhang, P., Xu, X., Wen, X. & Ran, Y., 2008a. Slip rates and recurrence intervals of the Longmen Shan active fault zone, and tectonic implications for the mechanism of the May 12 Wenchuan earthquake, 2008, Sichuan, China, *Chinese. J. Geophys. (in Chinese),* **51**(4), 1066–1073.

Zhang, Q., Sandvol, E., Ni, J., Yang, Y. & Chen, Y.J., 2011. Rayleigh wave tomography of the northeastern margin of the Tibetan Plateau, *Earth planet. Sci. Lett.,* **304**(1), 103–112.

Zhang, X., Yang, Z., Yang, Y., Yang, J., Song, J. & Zhao, P., 1995. Tomographic determination of 3-D crustal structure —joint inversion of explosion and earthquake data, *Earthq. Sci.,* **8**(4), 519–529.

Zhang, X. *et al.,* 2008b. Crustal structures beneath west Qinling-east Kunlun orogen and its adjacent area—result of wide-angle seismic reflection and refraction experiment, *Chinese. J. Geophys. (in Chinese),* **51**(2), 307–318.

Zhang, Y. & Zheng, J., 1994. *Geologic Overview in Kokshili, Qinghai and Adjacent Areas (in Chinese),* pp. 177, Seismological Publishing House.

Zhang, Z., Bai, Z., Klemperer, S., Tian, X., Xu, T., Chen, Y. & Teng, J., 2013. Crustal structure across NE Tibet from wide-angle seismic profiling: constraints on the Caledonian Qilian orogeny and its reactivation, *Tectonophysics,* **606,** 140–159.

Zhan, Y., Yang, H., Zhao, G., Zhao, L. & Sun, X., 2017. Deep electrical structure of crust beneath the Madongshan step area at the Haiyuan fault in the northeastern margin of the Tibetan plateau and tectonic implications, *Chinese. J. Geophys. (in Chinese),* **60**(6), 2371–2384.

Zhan, Y., Zhao, G.Z., Wang, L.F., Wang, J.J., Chen, X.B., Zhao, L.Q. & Xiao, Q.B., 2014. Deep electric structure beneath the intersection area of West Qinling orogenic zone with North-South Seismic tectonic zone in China, *Chinese. J. Geophys. (in Chinese),* **87**(z1), 425–426.

Zhao, D., 2015. *Multiscale Seismic Tomography,* pp. 304, Springer.

Zhao, D., Hasegawa, A. & Horiuchi, S., 1992. Tomographic imaging of P and S wave velocity structure beneath northeastern Japan, *J. geophys. Res.,* **97,** 19909–19928.

Zhao, D., Liu, X. & Hua, Y., 2018a. Tottori earthquakes and Daisen volcano: effects of fluids, slab melting and hot mantle upwelling, *Earth planet. Sci. Lett.,* **485,** 121–129.

Zhao, D., Todo, S. & Lei, J., 2005a. Local earthquake reflection tomography of the Landers aftershock area, *Earth planet. Sci. Lett.,* **235,** 623–631.

Zhao, D., Wang, Z., Umino, N. & Hasegawa, A., 2007. Tomographic Imaging outside a Seismic Network: application to the Northeast Japan Arc, *Bull. seism. Soc. Am.,* **97,** 1121–1132.

Zhao, D., Yamashita, K. & Toyokuni, G., 2018b. Tomography of the 2016 Kumamoto earthquake area and the Beppu-Shimabara graben, *Sci. Rep.,* **8,** 15488.

Zhao, G. *et al.,* 2005b. Relation between electricity structure of the crust and deformation of crustal blocks on the northeastern margin of Qinghai-Tibet Plateau, *Sci. China,* **48**(10), 1613–1626.

Zhao, J., Li, S., Zhang, X., Yang, Z., Zhang, C., Liu, B., Zhang, J. & Pan, S., 2005c. Three dimensional Moho geometry beneath the northeast edge of the Qinghai-Tibet Plateau, *Chinese. J. Geophys. (in Chinese),* **48**(1), 92–100.

Zheng, D., Li, H., Shen, Y., Tan, J., Ouyang, L. & Li, X., 2015. Crustal and upper mantle structure beneath the northeastern Tibetan Plateau from joint analysis of receiver functions and Rayleigh wave dispersions, *Geophys. J. Int.,* **204**(1), 583–590.

Zheng, Y., Yang, Y., Ritzwoller, M.H., Zheng, X., Xiong, X. & Li, Z., 2010. Crustal structure of the northeastern Tibetan plateau, the Ordos block and the Sichuan basin from ambient noise tomography, *Earthq. Sci.,* **23**(5), 465–476.

Zuza, A.V. & Yin, A., 2016. Continental deformation accommodated by non-rigid passive bookshelf faulting: an example from the Cenozoic tectonic development of northern Tibet, *Tectonophysics,* **677–678,** 227–240.

SUPPORTING INFORMATION

Supplementary data are available at *GJI* online.

Figure S1. (a) Histogram of traveltime residuals before the earthquake relocation. (b) Observed traveltimes with a reduced velocity of 6.5 km s^{-1} versus the epicentral distance before the earthquake relocation. The blue and green dots denote the P and PmP data, respectively. (c) Histogram of traveltime residuals (<2 s) for the events relocated with over eight traveltime data. (d) The same as (b) but for the selected events after relocation. (e) Reduced theoretical traveltimes computed with the TauP toolkit. The purple, red and black lines are for P, Pn and PmP arrivals, respectively. (f) Comparison of the observed traveltimes shown in (d) with the theoretical ones shown in (e).

Figure S2. A trade-off curve for determining the optimal value of the damping parameter (the red triangle).

Figure S3. Results of a checkerboard resolution test obtained by a joint inversion of the P and PmP wave data. The lateral grid interval is 0.5° × 0.5°. Open and solid circles denote slow and fast velocity anomalies, respectively, relative to the 1-D velocity model (the black line in Fig. 2a). The layer depth is shown at the upper-right corner of each map. The velocity perturbation scale (in per cent) is shown below (d).

Figure S4. The same as Fig. S3 but the lateral grid interval is 0.4° × 0.4°. The other labelling is the same as that in Fig. S3.

Figure S5. The same as Fig. S3 but the lateral grid interval is 0.35° × 0.35°. The other labelling is the same as that in Fig. S3.

Figure S6. The same as Fig. S5 but only the first P-wave data are used.

Figure S7. Results of a checkerboard resolution test along the two profiles shown in the inset map. The three curved lines in each vertical cross-section denote the Moho discontinuity and two velocity boundaries in the crust. The red star denotes the 1920 Haiyuan earthquake (M 8.5). The solid and open circles denote high and low velocity perturbations (in per cent), respectively, whose scale is shown at the bottom-right. The data used in the test are (a, d) P-wave arrivals, (b, e) PmP-wave arrivals, and (c, f) both P and PmP wave arrivals. The labelling of the inset map is the same as that in Fig. 1.

Please note: Oxford University Press are not responsible for the content or functionality of any supporting materials supplied by the authors. Any queries (other than missing material) should be directed to the corresponding author for the paper.